Measurement of Sub-micron Deformations and Stresses at Microsecond Intervals in Laterally Impacted Composite Plates Using Digital Gradient Sensing

C. Miao[1] · H. V. Tippur[1]

Abstract

Visualization and quantification of surface topography and stresses from measured slope data is of considerable importance to study many engineering problems including response of structural plates to stress wave loading. In this work, a full-field optical technique called Digital Gradient Sensing (DGS) is implemented in the reflection-mode to quantify time-resolved surface slopes in composite plates at microsecond intervals as they are impact loaded. The method being capable of determining two orthogonal surface slopes by measuring angular deflections of light rays, as small as a few micro-radians, surface topography can be quantified using a Higher-order Finite-difference-based Least-squares Integration (HFLI). Numerical differentiation of surface slopes, on the other hand, provides all three curvatures enabling estimation of stresses. Carbon fiber reinforced composite plates of different layups are subjected to dynamic impact loading using a Hopkinson pressure bar. Ultrahigh-speed digital photography is used to record deformations using DGS. The out-of-plane deformations are obtained by post-processing data from DGS at each time instant using HFLI whereas stresses are estimated by evaluating instantaneous curvatures obtained by differentiating measured slopes.

Keywords Composite plates · Impact loading · Vision-based measurements · Surface slopes · Deflections and stresses · Ultrahigh-speed photography

Introduction

The use of carbon fiber reinforced polymer (CFRP) composites as structural materials has increased substantially in the past few decades [1–3]. They are widely used in aerospace, automotive, and other transportation industries for both military and civilian purposes due to tailorable stiffness, strength, toughness and high energy absorption characteristics coupled with lightweight feature. Yet, these materials are rather susceptible to stress wave induced events leading to disbond formation and fiber/matrix damage due to shock and impact by projectiles, falling objects and/or flying debris during service. Thus compromised CFRP has undesirable reduction of strength and load-bearing capacity [4–6]. Hence, the ability to quantitatively visualize deformations of CFRP structures under dynamic impact conditions is critical for assuring mechanical integrity and safety.

Several optical techniques which offer full-field, non-contact measurements have been proposed and used for quantitative visualization of mechanical response of composite materials [7]. They can be broadly classified into coherent and incoherent methods based on the type of illumination used while performing measurements. Quinn et al. [8] investigated distribution of surface strains on 3D woven composites subjected to tensile loading using electronic speckle pattern interferometry (ESPI). The same method was employed in conjunction with embedded fiber optic sensors to study deformation behavior of cross-ply composite laminates under three-point bending by Bosia et al. [9]. Tippur et al. [10] proposed a lateral shearing interferometry, called the Coherent Gradient Sensing (CGS), which can be applied to measure real-time surface slopes of thin films and structures [11, 12]. Among the incoherent methods, techniques based on moiré phenomena

✉ H. V. Tippur
tippuhv@auburn.edu

1 Department of Mechanical Engineering, Auburn University, Auburn, AL 36849, USA

have been applied in several forms. Ritter [13] proposed the reflection moiré method to study the dynamic plate bending. Cairns et al. [14] studied the mechanical response of composite laminates under compression by using shadow moiré method. The same method was used by Karthikeyan et al. to study the ballistic response of laminated composite plates [15] undergoing large deformations and lamina failure. In recent years, Digital Image Correlation (DIC) methods have become very popular for measuring structural deformations [16–23]. Koerber et al. [16] conducted an investigation of transverse compression and in-plane shear properties of unidirectional polymer composites under quasi-static and dynamic loading by using 2D DIC. Yamada et al. [17] carried out 3D measurements to evaluate the mechanical performance of CFRP during rapid loading by using 3D DIC by employing two high-speed cameras to measure in-plane as well as out-of-plane deformations. Although using two high-speed cameras has its advantages, it increases the hardware cost and the complexity of the experimental setup including synchronization of the cameras and subsequent data analysis. Hence, 3D DIC approaches with a single high-speed camera have been introduced [18, 19]. Pan et al. [20] investigated the full-field transient 3D deformation of braided composites plates during ballistic impact by using 3D DIC with a single high-speed camera coupled with a clever light path modification.

Recently, a new full-field optical method called Digital Gradient Sensing (DGS) has been proposed by the authors for measuring small angular deflections of light rays caused by stresses in planar solids [21, 22]. Subsequently, extensions to DGS methodology to study optically reflective objects by measuring two orthogonal surface slopes [23] have been made. The simplicity of the experimental setup and its measurement accuracy along with the ubiquity of 2D image correlation algorithms make DGS attractive for measuring surface slopes as they can be integrated to evaluate deformed surface profiles or differentiated to assess curvatures. Jain et al. [24] reported on extending the reflection-mode DGS (or, r-DGS) to study transient deformations and damage in planar solids. Miao et al. [25] investigated the feasibility of r-DGS used in conjunction with a robust Higher-order Finite-difference-based Least-squares Integration (or simply HFLI) scheme to measure the surface topography of thin structures. The research reported in this article deals with quantitative visualization of deformations in the sub-micron and micron levels in CFRP made using r-DGS when used in conjunction with ultrahigh-speed photography enabling microsecond temporal resolution over relatively large regions-of-interest (ROI). These features are rather unique when compared to other methods which often rely on specialized optics and/or microscopy to perform measurements of this nature over small ROI.

In the following, the principles of r-DGS and HFLI are briefly described. Then, a calibration test using an isotropic plate, PMMA, subjected to dynamic impact is reported.
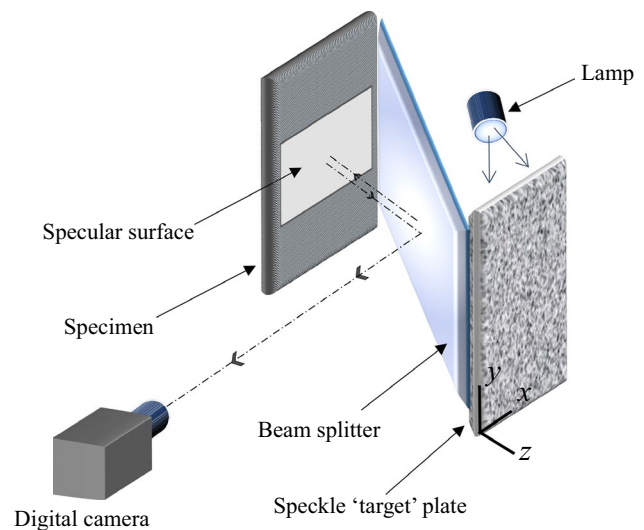

Fig. 1 Schematic of r-DGS experimental setup

Next, the full-field transient sub-micron and micron scale deformations of unidirectional and quasi-isotropic CFRP plates are measured at microsecond intervals. Finally, the major results on temporal evolution of surface profile and stresses are reported and results are summarized.

Reflection-mode Digital Gradient Sensing (r-DGS)

A schematic of the experimental setup for reflection-mode Digital Gradient Sensing (r-DGS) used to measure surface slopes is shown in Fig. 1. A digital camera is used here to record random speckles on the target plate via specularly reflective specimen surface. To accomplish this, the specimen and the target plate are placed parallel to each other, and a beam splitter is situated at 45° relative to the specimen and the target plate, respectively. The specimen surface is made reflective in this work using vapor deposition of aluminum film or the so-called film transfer technique [26] in which a vapor deposited thin film on a substrate is transferred to the surface of the specimen. The target plate is covered with black and white spray paint to create random speckles, and is illuminated uniformly using a broad spectrum white light source while recording.

A 2D schematic of r-DGS is shown in Fig. 2. For simplicity, the angular deflections of light rays in the y–z plane are illustrated. The normal distance between the target plate and the specimen surface is defined by Δ. When the specimen is in the undeformed state, a point P on the target plate is in focus via point O on the specimen surface. An image is recorded at this time instant/state as the reference image. After the specimen suffers out-of-plane deformation, a neighboring point Q on the target plate comes into focus through the same point on the specimen surface O. The
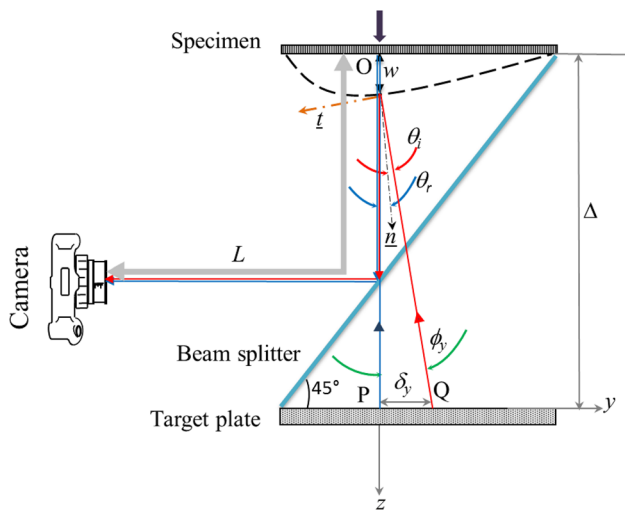
Fig. 2 2D schematic explaining the working principle of r-DGS

corresponding deformed image is recorded next. The line connectors OP and OQ make an angle $\phi_y, \phi_y = \theta_i + \theta_r$ where $\theta_i = \theta_r$ are the incident and reflection angles of light rays relative to the normal to the specimen surface. Then, the two local surface slopes can be calculated as $\frac{\partial w}{\partial y:x} = \frac{1}{2}\tan\left(\phi_{y:x}\right)$.

The local displacements $\delta_{y:x}$ can be obtained by performing a 2D image correlation of the reference and deformed images. The governing equations for r-DGS are [23]:

$$\frac{\partial w}{\partial y:x} = \frac{1}{2}\tan\left(\phi_{y:x}\right) \approx \frac{1}{2}\left(\phi_{y:x}\right) \approx \frac{1}{2}\left(\frac{\delta_{y:x}}{\Delta}\right). \tag{1}$$

It is important to note that the coordinates of the specimen plane are used in the above governing equations. However, the camera is focused on the target plane while recording random speckles. Accordingly, a mapping function needs to be used to transfer its coordinates to the specimen plane using a pin-hole camera approximation, $(x : y) = \frac{L}{L+\Delta}(x_0 : y_0)$ where $(x : y)$ and $(x_0 : y_0)$ represent the coordinates of the specimen and target planes, respectively, and L is the distance between the specimen and the camera lens [21].

Integration of Slope Data

Two orthogonal surface slopes in the form of a 2D rectangular array can be obtained from r-DGS. In many engineering applications, however, it is rather useful to quantify and visualize the surface profile or the surface topography instead of or in addition to the surface slopes. Therefore, it is valuable to reconstruct the deformed surface profile from r-DGS by post-processing measured slope data.

Surface topography reconstruction from measured slopes requires numerical integration of r-DGS measurements. This

can be achieved using least-squares analysis based 2D integration methods. Southwell proposed a Traditional Finite-difference-based Least-squares Integration or TFLI algorithm based on a rectangular grid configuration [27, 28]. The surface reconstruction values are computed at the same locations of measured orthogonal surface slopes in this method. The equations connecting the slopes and the reconstructed values as an $M \times N$ matrix in this approach are expressed as [25, 28],

$$\begin{cases} \frac{f_{m,n+1}-f_{m,n}}{x_{m,n+1}-x_{m,n}} = \frac{s^x_{m,n+1}+s^x_{m,n}}{2}, & \begin{aligned} m &= 1,2,...,M, \\ n &= 1,2,...,N-1. \end{aligned} \\ \frac{f_{m+1,n}-f_{m,n}}{y_{m+1,n}-y_{m,n}} = \frac{s^y_{m+1,n}+s^y_{m,n}}{2}, & \begin{aligned} m &= 1,2,...,M-1, \\ n &= 1,2,...,N. \end{aligned} \end{cases} \tag{2}$$

where x, y are the local coordinates, s denotes the local spatial gradients/slopes, f is the value of the function at (x, y). Equation (2) can be converted into a matrix form,

$$DF = G, \tag{3}$$

where

$$D = \begin{bmatrix} D^x \\ D^y \end{bmatrix} = \begin{bmatrix} -1 & 0 & \cdots & 0 & 1 & 0 & \cdots & \cdots & 0 \\ 0 & -1 & 0 & \cdots & 0 & 1 & 0 & \cdots & 0 \\ \vdots & \vdots & \vdots & \vdots & \vdots & \vdots & \vdots & \vdots & \vdots \\ 0 & \cdots & \cdots & 0 & -1 & 0 & \cdots & 0 & 1 \\ -1 & 1 & 0 & \cdots & \cdots & \cdots & \cdots & \cdots & 0 \\ 0 & -1 & 1 & 0 & \cdots & \cdots & \cdots & \cdots & 0 \\ \vdots & \vdots & \vdots & \vdots & \vdots & \vdots & \vdots & \vdots & \vdots \\ 0 & \cdots & \cdots & \cdots & \cdots & 0 & -1 & 1 \end{bmatrix}_{[M(N-1)+(M-1)N]\times MN} \tag{4}$$

$$F = \begin{bmatrix} f_{1,1} \\ f_{2,1} \\ \vdots \\ f_{M,N} \end{bmatrix}_{MN \times 1} \tag{5}$$

$$G = \begin{bmatrix} G^x \\ G^y \end{bmatrix} = \frac{1}{2} \begin{bmatrix} \left(s^x_{1,2}+s^x_{1,1}\right)\left(x_{1,2}-x_{1,1}\right) \\ \left(s^x_{2,2}+s^x_{2,1}\right)\left(x_{2,2}-x_{2,1}\right) \\ \vdots \\ \left(s^x_{M,N}+s^x_{M,N-1}\right)\left(x_{M,N}-x_{M,N-1}\right) \\ \left(s^y_{2,1}+s^y_{1,1}\right)\left(y_{2,1}-y_{1,1}\right) \\ \left(s^y_{3,1}+s^y_{2,1}\right)\left(y_{3,1}-y_{2,1}\right) \\ \vdots \\ \left(s^y_{M,N}+s^y_{M-1,N}\right)\left(y_{M,N}-y_{M-1,N}\right) \end{bmatrix}_{[M(N-1)+(M-1)N]\times 1} \tag{6}$$

Equation (3) can be solved to get F as,

$$F = \left(D^T D\right)^{-1} D^T G \tag{7}$$

where D^T denotes the transpose of D.

The TFLI method is widely used due to its simplicity. However, there is an algorithmic error of $O(h^3)$ where h indicates the interval between two adjacent grid points used in Taylor's expansion as noted by Li et al. [29]. A more accurate approach is proposed by incorporating higher order terms in the Taylor's expansion and two additional neighboring slopes into the integration scheme resulting in an algorithmic error of $O(h^5)$. This approach is entitled the Higher-order Finite-difference-based Least-squares Integration or the HFLI method. In this method, the G matrix is expressed as:

$$G = \begin{bmatrix} G^x \\ G^y \end{bmatrix} \tag{8}$$

$$G^x = \frac{1}{24} \begin{bmatrix} 12\left(s_{1,2}^x + s_{1,1}^x\right)\left(x_{1,2} - x_{1,1}\right) \\ 12\left(s_{2,2}^x + s_{2,1}^x\right)\left(x_{2,2} - x_{2,1}\right) \\ \vdots \\ 12\left(s_{M,2}^x + s_{M,1}^x\right)\left(x_{M,2} - x_{M,1}\right) \\ \left(-s_{1,4}^x + 13s_{1,3}^x + 13s_{1,2}^x - s_{1,1}^x\right)\left(x_{1,3} - x_{1,2}\right) \\ \left(-s_{2,4}^x + 13s_{2,3}^x + 13s_{2,2}^x - s_{2,1}^x\right)\left(x_{2,3} - x_{2,2}\right) \\ \vdots \\ \left(-s_{M,4}^x + 13s_{M,3}^x + 13s_{M,2}^x - s_{M,1}^x\right)\left(x_{M,3} - x_{M,2}\right) \\ \left(-s_{1,5}^x + 13s_{1,4}^x + 13s_{1,3}^x - s_{1,2}^x\right)\left(x_{1,4} - x_{1,3}\right) \\ \vdots \\ \left(-s_{M,5}^x + 13s_{M,4}^x + 13s_{M,3}^x - s_{M,2}^x\right)\left(x_{M,4} - x_{M,3}\right) \\ \vdots \\ \left(-s_{M,N}^x + 13s_{M,N-1}^x + 13s_{M,N-2}^x - s_{M,N-3}^x\right)\left(x_{M,N-1} - x_{M,N-2}\right) \\ 12\left(s_{1,N}^x + s_{1,N-1}^x\right)\left(x_{1,N} - x_{1,N-1}\right) \\ 12\left(s_{2,N}^x + s_{2,N-1}^x\right)\left(x_{2,N} - x_{2,N-1}\right) \\ \vdots \\ 12\left(s_{M,N}^x + s_{M,N-1}^x\right)\left(x_{M,N} - x_{M,N-1}\right) \end{bmatrix}_{[M(N-1)]\times 1} \tag{9}$$

$$G^y = \frac{1}{24} \begin{bmatrix} 12\left(s_{2,1}^y + s_{1,1}^y\right)\left(y_{2,1} - y_{1,1}\right) \\ \left(-s_{4,1}^y + 13s_{3,1}^y + 13s_{2,1}^y - s_{1,1}^y\right)\left(y_{3,1} - y_{2,1}\right) \\ \left(-s_{5,1}^y + 13s_{4,1}^y + 13s_{3,1}^y - s_{2,1}^y\right)\left(y_{4,1} - y_{3,1}\right) \\ \vdots \\ \left(-s_{M-1,1}^y + 13s_{M-2,1}^y + 13s_{M-3,1}^y - s_{M-2,1}^y\right)\left(y_{M-2,1} - y_{M-3,1}\right) \\ 12\left(s_{M,1}^y + s_{M-1,1}^y\right)\left(y_{M,1} - y_{M-1,1}\right) \\ 12\left(s_{2,2}^y + s_{1,2}^y\right)\left(y_{2,2} - y_{1,2}\right) \\ \left(-s_{4,2}^y + 13s_{3,2}^y + 13s_{2,2}^y - s_{1,2}^y\right)\left(y_{3,2} - y_{2,2}\right) \\ \vdots \\ \left(-s_{M-1,2}^y + 13s_{M-2,2}^y + 13s_{M-3,2}^y - s_{M-2,2}^y\right)\left(y_{M-2,2} - y_{M-3,2}\right) \\ 12\left(s_{M,2}^y + s_{M-1,2}^y\right)\left(y_{M,2} - y_{M-1,2}\right) \\ 12\left(s_{2,3}^y + s_{1,3}^y\right)\left(y_{2,3} - y_{1,3}\right) \\ \left(-s_{4,3}^y + 13s_{3,3}^y + 13s_{2,3}^y - s_{1,3}^y\right)\left(y_{3,3} - y_{2,3}\right) \\ \vdots \\ 12\left(s_{M,N}^y + s_{M-1,N}^y\right)\left(y_{M,N} - y_{M-1,N}\right) \end{bmatrix}_{[(M-1)N]\times 1}$$

Miao et al. [25] have recently showed the feasibility of surface topography reconstruction from r-DGS output by using HFLI.

Calibration

The dynamic impact of a PMMA plate was studied using r-DGS in conjunction with ultrahigh-speed digital photography using a single sensor camera. A 152.4 mm × 101.6 mm rectangular PMMA specimen of 8.5 mm thickness was used in the experiment. A 152.4×101.6 mm^2 face of the specimen was deposited with a thin aluminum film to make the surface reflective. The schematic of the experimental setup used is shown in Fig. 3. A modified Hopkinson pressure bar (or simply a 'long-bar') was used for loading the uncoated backside of the specimen. The long-bar was a 1.83 m steel rod of 25.4 mm diameter with a conical tip of 3 mm diameter impacting the backside of the specimen. A 305 mm long, 25.4 mm diameter steel striker placed in the barrel of a gas-gun was co-axially aligned with the long-bar at the start of the experiment. The striker was launched towards the long-bar at a velocity of ~8.5 m/s during tests. The corresponding strain history during impact loading event was measured by a strain gage affixed to the long-bar. The specimen was clamped using a fixture containing two steel plates with circular apertures, see Fig. 3. The apertures were 63.5 mm in diameter and coaxial facilitating optical measurements over a relatively large ROI. Loading point was at the center of the aperture. A beam splitter and the speckle target plate were placed in a 45° holder, housed within the cage of the specimen holding fixture, so that the speckle pattern on the target plate could be viewed via the reflective face of the specimen. The deformations on the front surface of the specimen were photographed by a Kirana-05M ultrahigh-speed digital camera assisted by a pair of Cordin-659 high energy flash lamps to illuminate the target. This camera is a single sensor camera, capable of recording 10-bit gray scale images at a maximum rate of 5 million frames per second and at a spatial resolution of 924 × 768 pixels per image. The camera and the two flash lamps were triggered using a variable delay circuit relative to the time instant the striker impacts the long-bar and the duration required for the stress waves to travel a length of 1.83 m along the steel rod.

A Nikon 70–300 mm focal length macro zoom lens with an adjustable bellows was used with the camera to record the images. A good exposure and focus were achieved by stopping down the lens aperture to F/8.0 after focusing. The distance between the specimen and the camera lens plane (L) was ~950 mm and the one between the specimen mid-plane and the target plane (Δ) was 102 mm. A total of 180 images, some in the undeformed state and others in the deformed state, were recorded at 1 million frames per second. When the long-bar was impacted by the striker, a compressive stress wave was generated that propagated along the bar. The fixture/cage used to house the specimen was mounted on a pair of guide-rails so that it can slide away from the long-bar when the specimen was loaded by the stress waves. However, the inertia of the fixture was substantially higher than that of the specimen and hence it took several milliseconds for the fixture to move away from the long-bar whereas the images corresponding to specimen deformations were recorded over approx. 100 microseconds. Thus, the specimen was nominally in contact with the long-bar throughout the measurement history. Four select speckle images at different time instants are shown in Fig. 4. In these, $t = 0$ μs corresponds to the start of the loading event on the plate. The distortion of the speckles due to the out-of-plane deformation evident in the central part of the images is caused by the out-of-plane deformations of the PMMA plate. However, no distortion of speckles can be observed in the image at $t = 5$ μs as out-of-plane deformation of the PMMA plate is extremely small to discern using naked eyes. One undeformed image just before the start of deformation was selected as the reference image. Subsequent deformed images were correlated with the reference image by using ARAMIS® image analysis software. During image correlation, a sub-image size of 40 × 40 pixels (1 pixel = 83.31 μm) with 30 pixels overlap was used to extract the local displacements $\delta_{y:x}$ in the ROI. In order to achieve correlation over the entire image and over the deformation range, a relatively large sub-image size was selected in favor of smaller sub-images.[1] The displacement fields were then used to compute the two orthogonal angular deflection fields of light rays ($\phi_{y:x}$).

The time-resolved orthogonal surface slope contours $\frac{\partial w}{\partial x}$ and $\frac{\partial w}{\partial y}$ due to stress wave propagation in the PMMA plate are shown in Fig. 5 at a few select time instants. The unreformed/reference image mentioned earlier was selected from a sequence of 10–20 images recorded before the start of the impact event or $t = 0$ μs. Once the compressive stress wave from the long-bar enter the PMMA plate, the impact induced stress waves propagate through the plate thickness (8.5 mm) from the contact point to reach the outer (recorded) surface of the plate. During the early stages of impact, deformations are concentrated close to the center of the plate (chosen as the origin) resulting in small surface slopes and sparse contours. The rest of the plate is undeformed as stress waves are

---

[1] The role of sub-image size in the range 20 × 20 to 40 × 40 pixels, each with the same step size, on the measurement of angular deflections are included in "Appendix" (Fig. 22: 1) for a time instant t = 15 μs for completeness. Magnitude of maximum slope difference between 20 × 20 and 40 × 40 sub-image size choice was approx. 6.1%. The larger sub-image size results in a smaller magnitude slope relative to smaller sub-image due to smoothing effect. The latter produces noisier variation of slopes relative to the former.
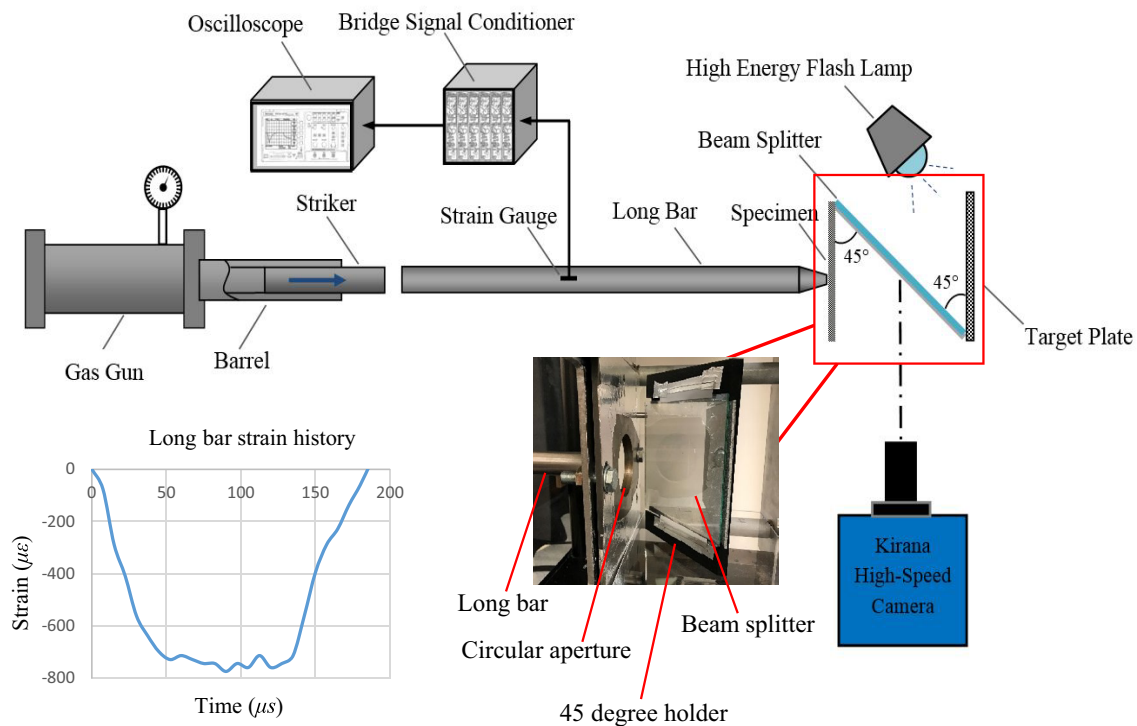
Fig. 3 Schematic of the experimental setup for dynamic plate impact study. Insets show the close-up of the optical arrangement and the strain history due to the compressive pulse measured on the Hopkinson bar

yet to reach those outer regions and hence surface slopes are vanishingly small, below the measurement sensitivity of the method. With the passage of time, the contours get denser and larger with a higher concentration of contours near the contact point. The vertical line of symmetry in $\frac{\partial w}{\partial x}$ contours and the horizontal line of symmetry in $\frac{\partial w}{\partial y}$ contours indicate the zero surface slope as to be expected of the single point impact at the center of the plate. The contours of $\left(\frac{\partial w}{\partial r} = \sqrt{ \left(\frac{\partial w}{\partial x} \right)^2 + \left(\frac{\partial w}{\partial y} \right)^2 } \right)$ are also shown in Fig. 6, where r is the radial distance from the contact point. These show very high degree of axisymmetry and also a higher concentration of contours near the impact point which become relatively sparse first before becoming dense again in the area away from the origin. This is because the slopes $\frac{\partial w}{\partial r}$ vary substantially in the regions around the impact point and near the clamped edge, while they are nearly constant in the intermediate region.

The reconstructed 3D surfaces computed through 2D integration using slope data from r-DGS in conjunction with HFLI algorithm are plotted in Fig. 7. The corresponding contours of out-of-plane displacements (w) at 1 μm increment are shown in Fig. 7b, d, f. It can be observed that the out-of-plane deformations are very small in the early stages

of impact, and they increases with time. The circular contours in the right column demonstrate that the reconstructed shape matches very well with the reality of the experiment both qualitatively and quantitatively.

The surface slope contours $\frac{\partial w}{\partial x}$ and $\frac{\partial w}{\partial y}$ at $t = 2$ μs are plotted in Fig. 8a, b. The contour increments here are 1×10^{-5} rad (or $\sim 5.7 \times 10^{-4}$ deg.), approx. equal to the generally accepted 1% of the pixel accuracy limit of DIC method. Hence, the experimental noise is somewhat more evident in the figure relative to the one in Fig. 5. However, at the center of the figure, slope contours can be clearly discerned. After integrating the surface slope data using the HFLI scheme, the reconstructed 3D surface and the corresponding contour representation of out-of-plane displacements (w) in 50 nm increments are plotted in the second row (Fig. 8c, d). Unlike differentiation, the numerical integration of measured data produces a smoothing effect on the resulting out-of-plane displacements. More importantly, deformation in the sub-micron scale ($w \sim 190$ nm) are discernible using r-DGS when used in conjunction with the HFLI algorithm. The circular contours at the bottom right figure also demonstrate that the reconstructed shape qualitatively matches well with the reality of the experiment.
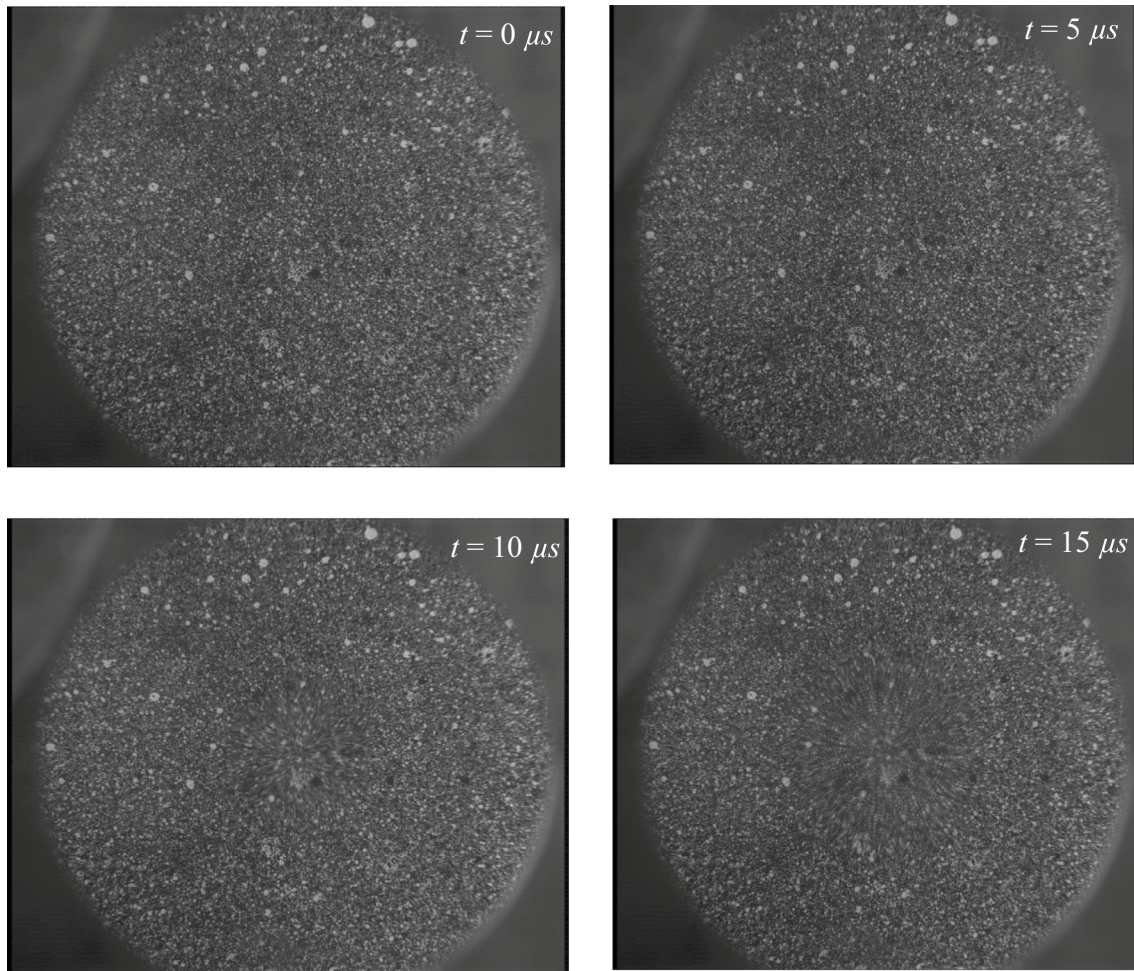
Fig. 4 Recorded speckle images from ultrahigh-speed camera at different time instants. The nominal diameter of the region of interest is 63.5 mm. Disturbance to the recorded speckles is readily evident in the last two images relative to the one at $t = 0$ μs

The out-of-plane deformations along $x = 0$ at a few select time instants are plotted in Fig. 9.[2] The radius R was measured from the impact point. In all the cases, due to stress wave propagation through the plate thickness from the impact point to reach the observed surface of the plate, the out-of-plane deformations emanate from the contact point and propagate outwards towards the clamped edge. It was observed that the out-of-plane deformations monotonically increase but somewhat rapidly after 6 μs.

Since r-DGS is able to measure instantaneous orthogonal surface slopes $\frac{\partial w}{\partial x}$ and $\frac{\partial w}{\partial y}$ in the entire field, evaluation of instantaneous curvatures $\frac{\partial^2 w}{\partial x^2}$, $\frac{\partial^2 w}{\partial y^2}$ and $\frac{\partial^2 w}{\partial x \partial y}$ require just one

additional differentiation of the measured data[3]. Now, by recognizing that stresses in thin plates are related to curvatures in Kirchhoff plate theory [30] as,

$$
\begin{pmatrix} \sigma_{xx} \\ \sigma_{yy} \\ \sigma_{xy} \end{pmatrix} = \begin{bmatrix} C_{11} & C_{12} & C_{13} \\ C_{21} & C_{22} & C_{23} \\ C_{31} & C_{32} & C_{33} \end{bmatrix} \begin{pmatrix} \varepsilon_{xx} \\ \varepsilon_{yy} \\ 2\varepsilon_{xy} \end{pmatrix} = -z \begin{bmatrix} C_{11} & C_{12} & C_{13} \\ C_{21} & C_{22} & C_{23} \\ C_{31} & C_{32} & C_{33} \end{bmatrix} \begin{pmatrix} \frac{\partial^2 w}{\partial x^2} \\ \frac{\partial^2 w}{\partial y^2} \\ 2\frac{\partial^2 w}{\partial x \partial y} \end{pmatrix}
$$

$$(10)$$

where C_{ij} (i, j = 1,…,3) are the elements of the stiffness matrix for the material. Under the assumption that the functional form of Kirchhoff plate theory holds for transient

---

[2] The role of the sub-image size (20×20 to 40×40 pixels) on the out-of-plane deformation is included in "Appendix" (Fig. 22: 2) for a time instant $t = 15$ μs for completeness. The differences between the maximum displacement estimates however reduce significantly ($< 1\%$) when integrated using HFLI.

[3] As it is well known that differentiation exaggerates noise in the experimental data, single differentiation is obviously very desirable instead of performing two successive differentiations of measured out-of-plane deformations as it would be case in, say, 3D-DIC or shadow moiré methods, a subtle but significant issue for estimating stresses.
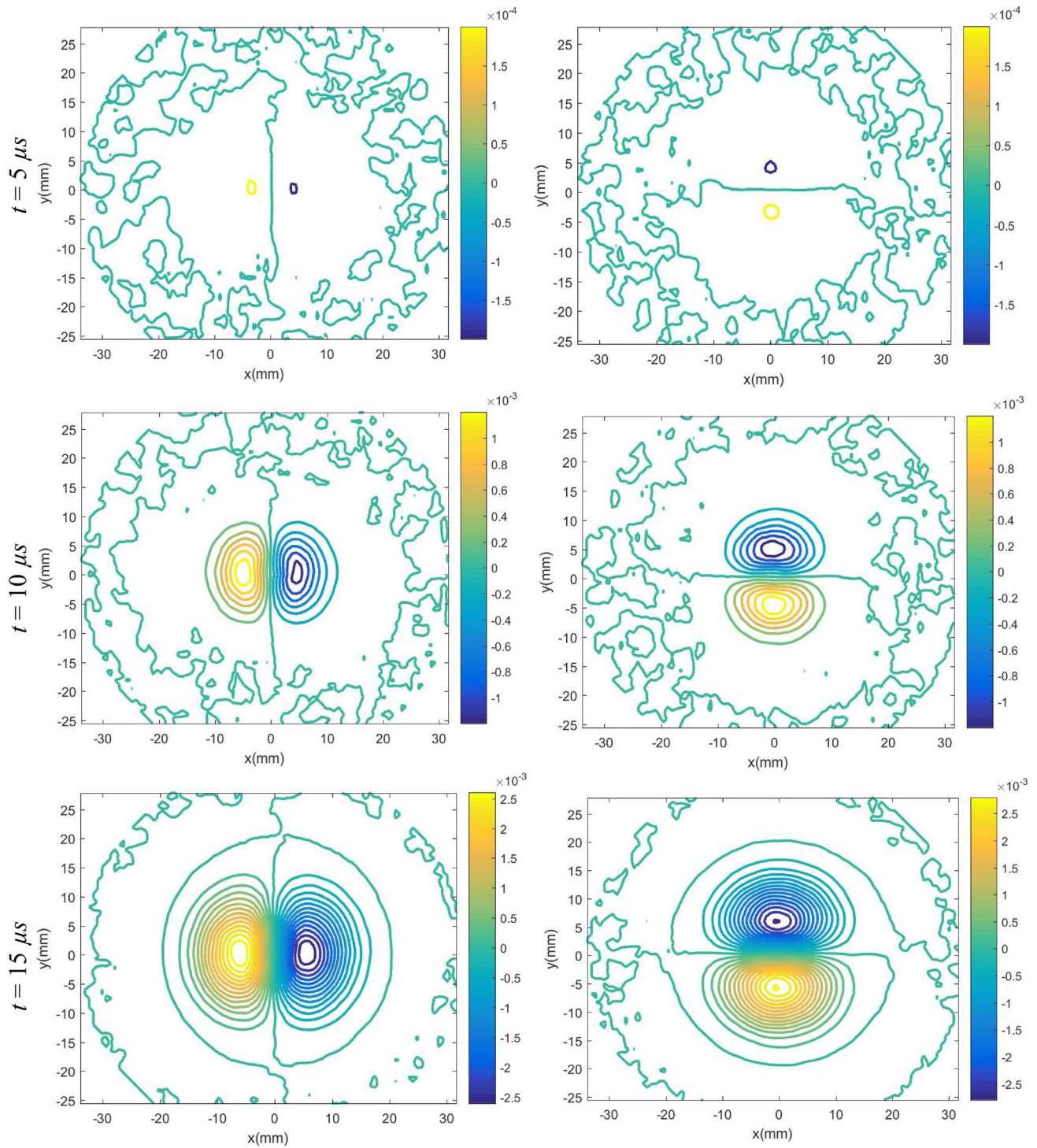
Fig. 5 Evolution of surface slope $w_{,x}$ (left column) and $w_{,y}$ (right column) contours for a clamped PMMA plate subjected to central impact. The impact point is made to coincide with (0, 0); contour increments $= 2 \times 10^{-4}$ rad
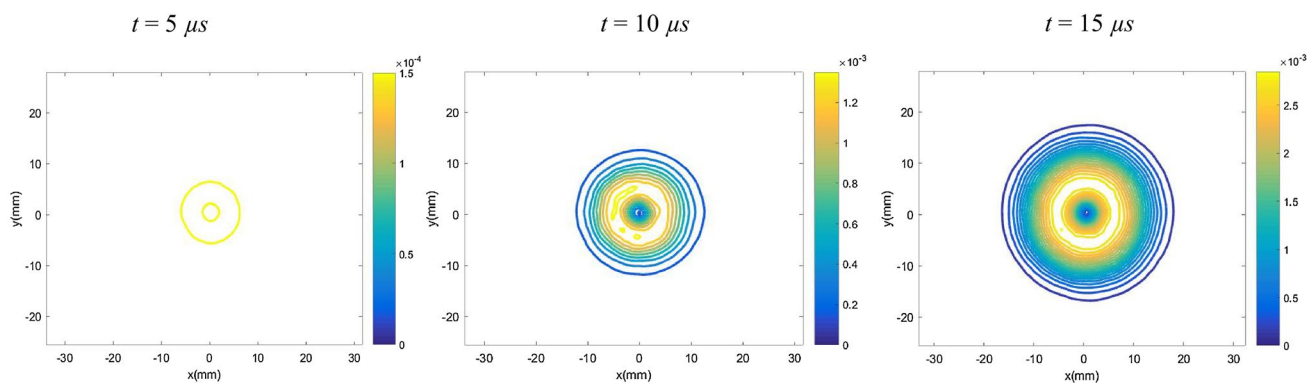
Fig. 6 Evolution of surface slope $w_{,r}$ contours for a clamped PMMA plate subjected to central impact. The impact point is made to coincide with (0, 0); contour increments $= 1.5 \times 10^{-4}$ rad

conditions, instantaneous stresses were estimated. That is, the slope data was differentiated using central difference scheme[4] to obtain local curvatures and the corresponding stresses over the entire ROI. Thus estimated values of σ_{xx} and σ_{xy} at $t = 20$ μs are plotted in Fig. 10 as stress surfaces. (The σ_{yy} plots are avoided here for brevity due to its similarity with σ_{xx} field but rotated by 90°.) The distribution of normal stress σ_{xx}, approaching a tensile peak ($\sim 280 \pm 18$ MPa) at the origin.[5] The tensile stresses rapidly decrease into a torus shaped valley of compressive stresses before becoming negligibly small far away from the impact point. The shear stress distribution of σ_{xy}, on the other hand, is skewed along $\pm 45°$ directions with dual equidistant positive and negative peaks away from the origin.

To complement the experimental results, a 3D elasto-dynamic finite element simulation was carried out using ABAQUS® structural analysis software. A quarter-model, as shown in Fig. 11, was simulated. The specimen and the end of steel long-bar were discretized into 202,215 and 7580 eight-node hexahedral elements, respectively. The regions corresponding to the clamped region were restrained in the out-of-plane direction and a kinematic contact condition was imposed between the PMMA plate and the tip of the steel long-bar. The dynamic elastic modulus (4.92 GPa) and

Poisson's ratio (0.32) of PMMA were used in the simulation based on ultrasonic measurement of longitudinal and shear wave speeds [31]. The elastic properties of 1144 carbon steel were used in the simulation of the long-bar (see Table 1). The particle velocity history ($V = c\varepsilon$, where c is the bar wave speed of steel and ε the strain), obtained from a measured strain gage history on the long-bar during the experiment, was used as an input in the numerical simulations. The out-of-plane displacements along the radius in the region-of-interest were extracted every 5 μs to compare with the corresponding results of the reconstructed 3D surface in Fig. 12. The solid lines represent values from numerical simulations and the solid symbols are the experimental counterparts. It can be observed that there is a rather good agreement between the two data sets. Moreover, the ability of the methodology to detect sub-micron deformations at microsecond temporal resolution is evident and noteworthy.

CFRP Plates Under Dynamic Impact[6]

Two types of CFRP plates subjected to dynamic impact were studied next. One was an orthotropic CFRP plate made of T800s/3900-2 unidirectional laminate with a $[0_{24}]$ lay-up, the second was a quasi-isotropic CFRP plate made of the

---

[4] The role of the sub-image size (20×20 to 40×40 pixels) on the stress estimation is included in "Appendix" (Fig. 22: 3) for a time instant $t = 15$ μs for completeness. A difference in the peak value of stress σ_{xx} of approx. 13% is evident between the smallest and the largest sub-image size. Furthermore, two types of central difference schemes, one with an algorithmic error of $O(h^2)$ and another $O(h^4)$ where h is the step-size, were attempted. A representative result at a time instant $t = 15$ μs is shown in "Appendix", Fig. 23.

[5] Note that the peak stress cannot be evaluated precisely due to numerical differentiation errors and the finite sub-image size used during image analysis. These, however, can be expected to greatly improve with the advent of higher pixel count sensors of smaller pixel size and better fill-factor in high-speed cameras.

[6] The effects of sub-image size on surface slopes, out-of-plane deformation and stresses for CFRP were studied along the lines described for PMMA. The corresponding results are shown in "Appendix" (Fig. 24: 1–3). The maximum (magnitude) slope difference between 20×20 and 40×40 sub-image size choice was approx. 6.9%. The larger sub-image size results in a smaller magnitude slope relative to smaller sub-image. The latter produces noisier variation of slopes relative to the former. As in case of PMMA, the differences in maximum out-of-plane deformations are significantly reduced ($< 0.5\%$) upon numerical integration of the slope data whereas maximum stress σ_{xx} (along the fibers) shows 3.5% difference between 20×20 and 40×40 sub-image size.
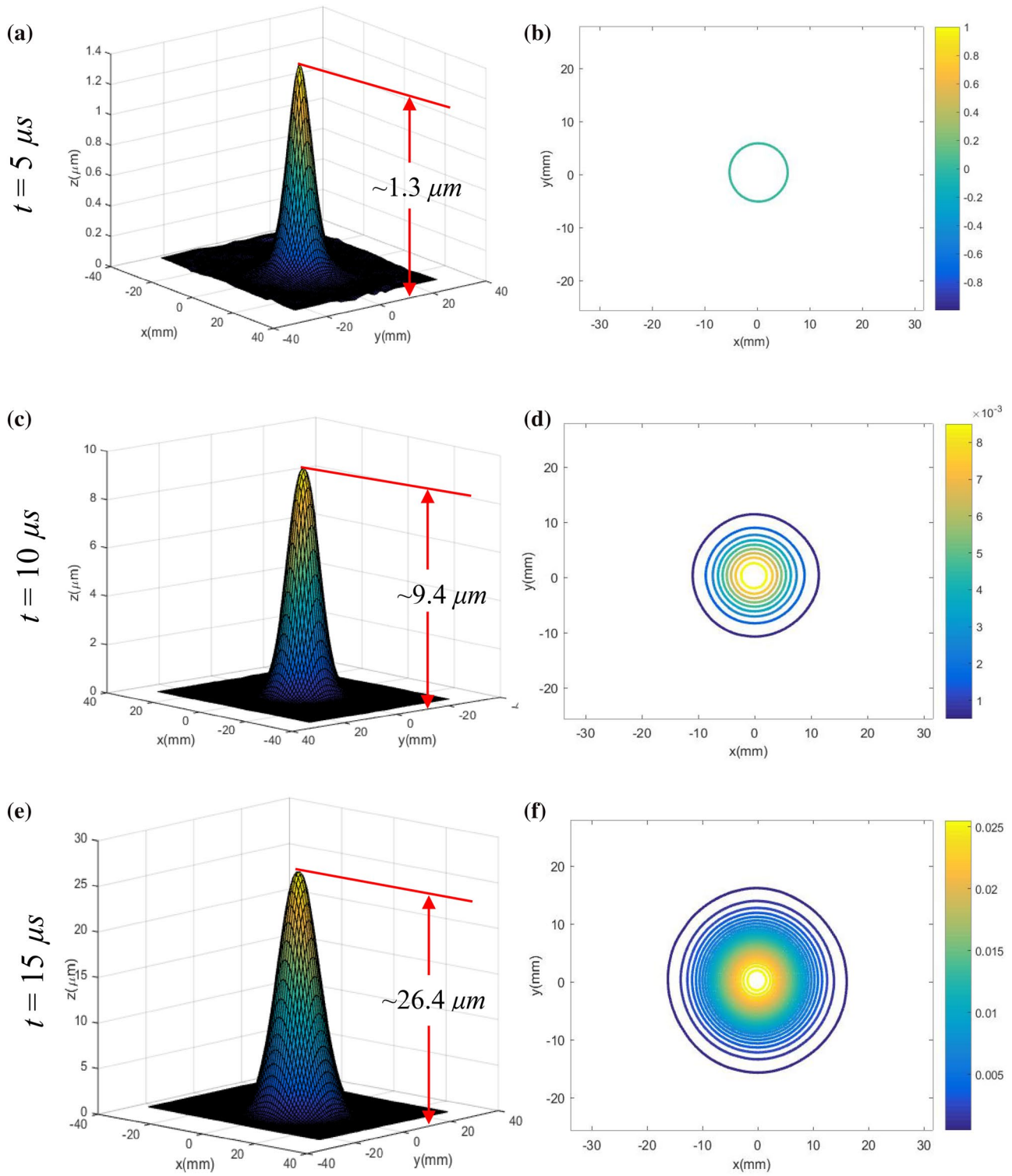
Fig. 7 Evolution of surface profile of PMMA plate at select time instants. Left column: reconstructed 3D surface; right column: out-of-plane displacement (w) contours (1 μm increment). The impact point is made to coincide with (0, 0)
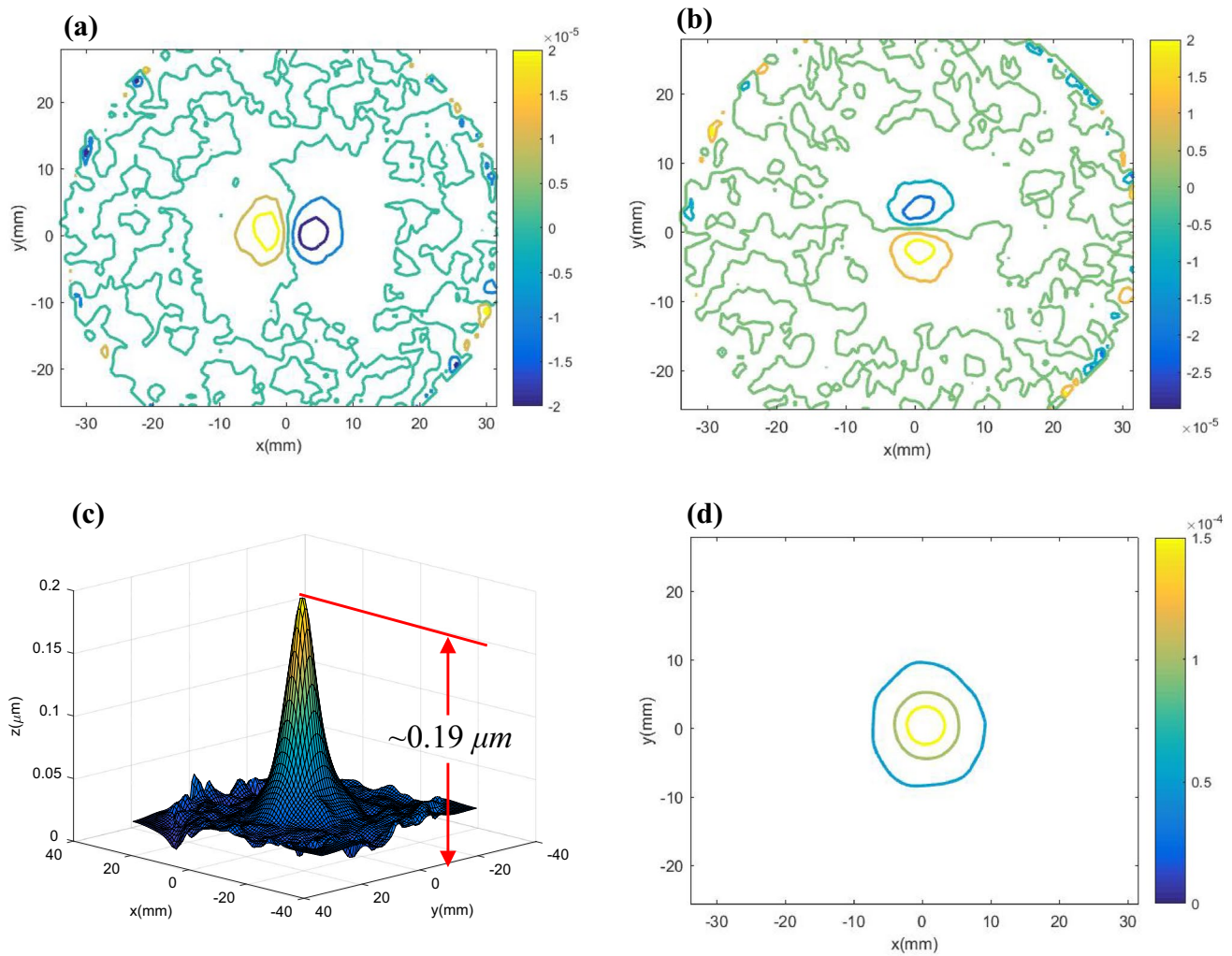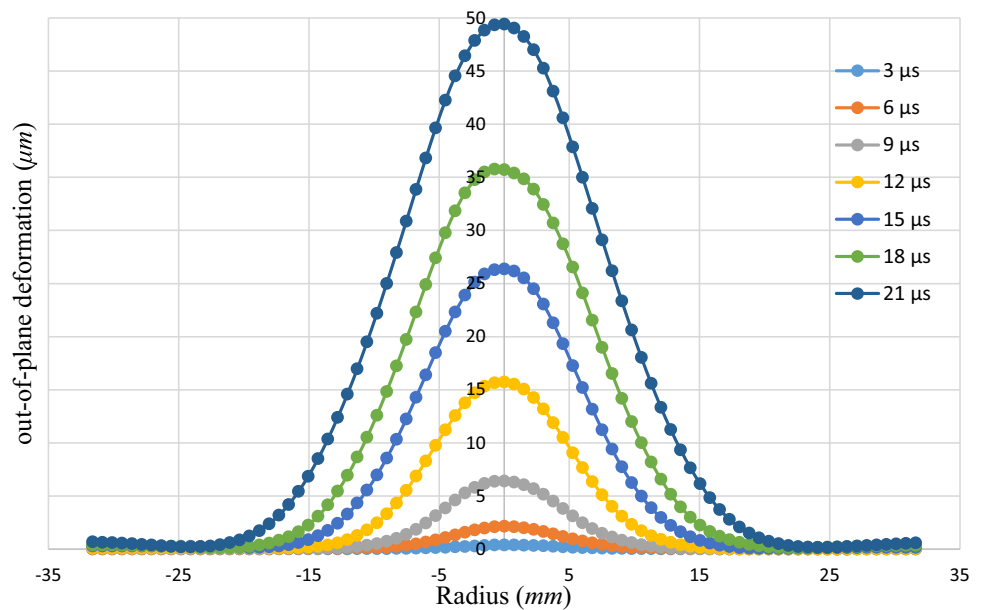
Fig. 8 Results for a clamped PMMA plate subjected to central impact at $t = 2\mu s$. Row 1: $w_{,x}$ (left) and $w_{,y}$ (right) contours; row 2: reconstructed 3D surface (left) and out-of-plane displacement (w) contours at 0.05 μm increment (right). The impact point is made to coincide with (0, 0)

Fig. 9 The measured transient profiles for a clamped PMMA plate subjected to central impact (see "Appendix" for error estimates)

$t = 20\ \mu s$
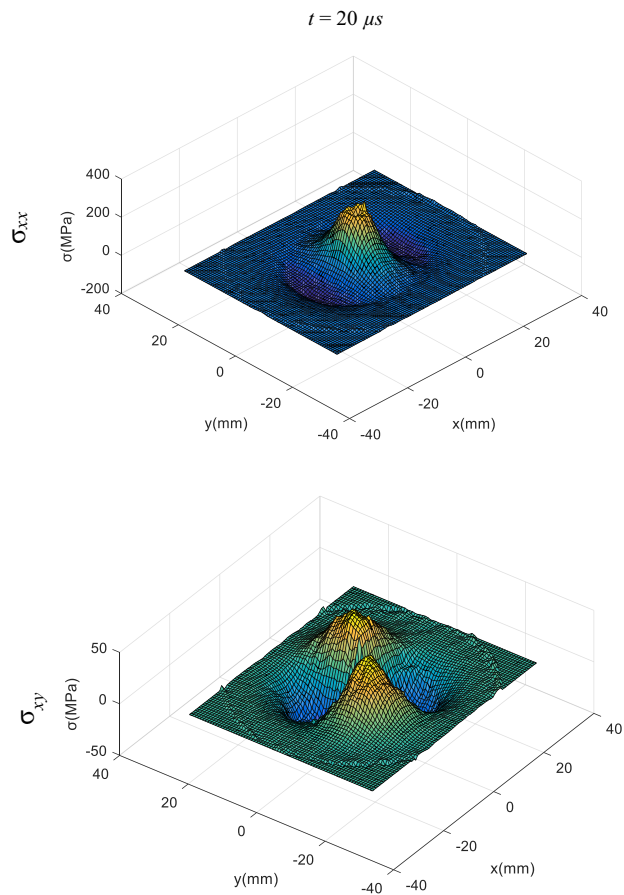
Fig. 10 Estimated stresses for a circular clamped PMMA plate subjected to central impact

Fig. 11 3D finite element model used for simulating impact on a clamped PMMA plate

same unidirectional laminae in $[(+45/90/-45/0)_3]$s lay-up (Toray Composite America, Inc.). For the unidirectional CFRP plate subjected to impact, the fiber direction coincided with the horizontal axis. The plate specimens were 152.4 mm × 101.6 mm × 4.5 mm made specularly reflective by using the aluminum film transfer technique. As in case of PMMA, the plates were clamped in the fixture beyond 63.5 mm diameter. A striker velocity of ~ 8.5 m/s was used in these experiments as well. A total of 180 images in the undeformed and deformed states were recorded at 1 million frames per second.

Unidirectional CFRP Plate

The time-resolved orthogonal surface slope contours representing $\frac{\partial w}{\partial x}$ and $\frac{\partial w}{\partial y}$ due to transient stress wave propagation in the unidirectional CFRP plate are shown in Fig. 13 at a few select time instants. Unlike PMMA plates, the slope contours here are visibly stretched in the horizontal direction, which corresponds to the fiber direction of this unidirectional composite along which the stress waves propagate
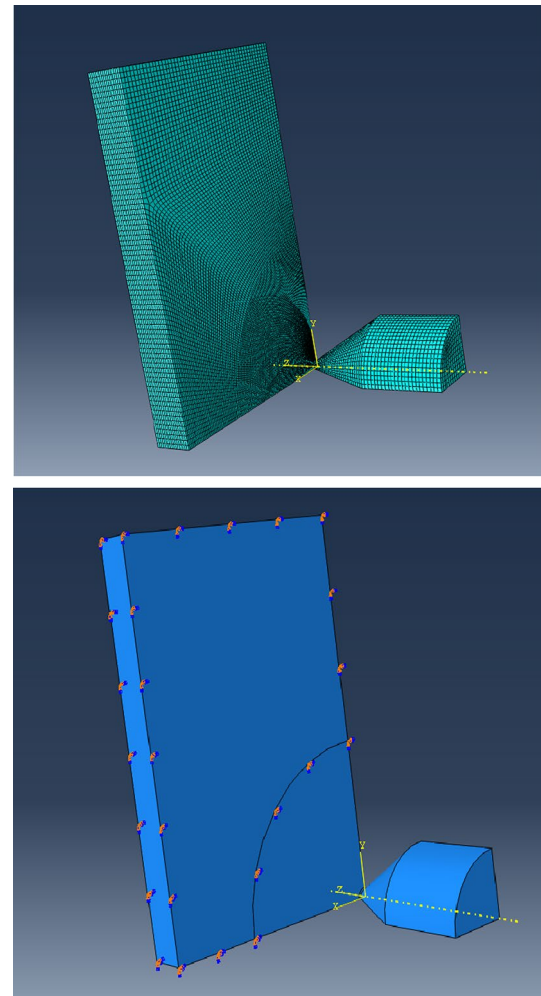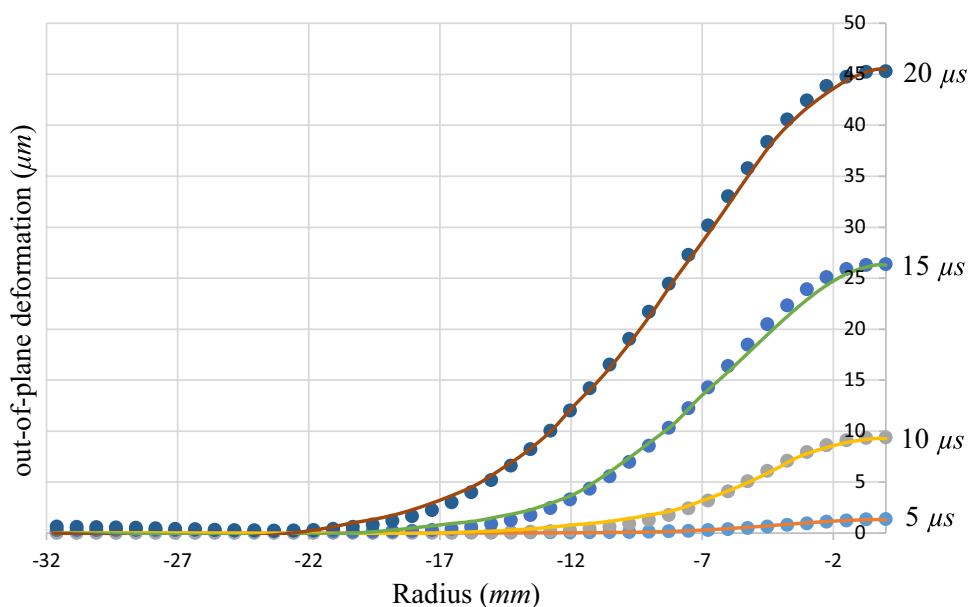
faster relative to the normal to the fiber direction. At $t = 15\ \mu s$, the outermost discernable contour corresponding to the zero surface slope is nearly rectangular in shape in contrast to the one for PMMA (see Fig. 5), which are circular due to isotropy. The reconstructed 3D surfaces obtained via 2D integration of surface slope data from r-DGS in conjunction with HFLI scheme are plotted in Fig. 14. The corresponding contours of out-of-plane displacements (w) at 0.8 μm increments are shown in Fig. 14b, d, f. A sub-micron deformation of 0.7 μm can be observed at $t = 5\ \mu s$. The oblong contours in Fig. 14b, d, f demonstrate that the reconstructed shape is qualitatively consistent with the reality of the experiment. The cross-sectional out-of-plane deformations, along and normal to the fiber directions, at a few select time instants are plotted in Fig. 15. The radius R here again is measured from the impact point, (0, 0). It can be observed that the radial extent of the out-of-plane deformations perpendicular to the fiber direction is narrower than the ones

Table 1 Material properties of 1144 carbon steel and PMMA used in finite element simulations

	1144 carbon steel	PMMA
Density (kg/m³)	7870	1100
Elastic modulus (GPa)	200	4.92
Poisson's ratio	0.29	0.32

along fiber direction, consistent with the reality of the experiment.

As in case of the PMMA plate, transient values of stresses in unidirectional CFRP were obtained. Thus estimated distribution of σ_{xx}, σ_{yy} and σ_{xy} at $t = 20$ μs are plotted in Fig. 16 as stress surfaces. These are relatively noisy when compared to the corresponding PMMA ones due to the fibrous nature of the composite besides numerical differentiation of slopes to obtain curvatures. Furthermore, the directionality of stress magnitudes is also readily evident in these plots. At this time instant, the normal stress σ_{xx} distribution approaches a tensile peak of ~3500 MPa at the origin. These stresses rapidly decay to compressive values before becoming negligibly small far away from the impact point. The distribution of normal stress σ_{yy} perpendicular to the fibers, on the other hand, also approaches a tensile peak of ~350 MPa at the origin, an order of magnitude lower than that for σ_{xx}. This too decays, but slowly normal to the fibers versus more steeply along the fibers, to compressive values before becoming negligible far away from the impact point. The shear stress σ_{xy} distribution is again skewed relative to the x-y axes, with two positive and negative peaks of ~65 MPa magnitude occurring along approximately ±45° directions away from the origin in the surface plot.

The experimental results obtained above are complemented using a 3D elasto-dynamic finite element simulation carried out using ABAQUS® structural analysis software. As in the PMMA plate case, a quarter-model (not shown for brevity) was simulated. The specimen and the end of steel long-bar were discretized into 511,608 and 7620 eight-node hexahedral elements, respectively. Kinematic contact was imposed between the CFRP plate and the steel long-bar tip. The material properties of CFRP used in these simulations are listed in Table 2 [32]. The out-of-plane displacements were extracted every 5 μs to compare with the corresponding experimental results (see Fig. 17). The solid lines represent values from the numerical simulation, and the solid symbols are from the experiment. It can be observed that there is a reasonably good agreement between the two data sets, demonstrating the feasibility of r-DGS and HFLI based measurements made during the dynamic impact experiment. It should also be noted that somewhat larger deviations between the two data sets is attributed to elastic properties used in the simulations as they were not measured by the authors but borrowed from a published report under quasi-static loading conditions.

Quasi-Isotropic CFRP Plate

Lastly, the time-resolved orthogonal surface slope contours of $\frac{\partial w}{\partial x}$ and $\frac{\partial w}{\partial y}$ during stress wave propagation in the quasi-isotropic CFRP plate are shown in Fig. 18 at a few select time instants. It can be observed that the contours here are somewhat similar to those of PMMA due to quasi-isotropy. The reconstructed 3D surfaces computed through 2D integration of surface slope data from r-DGS used in
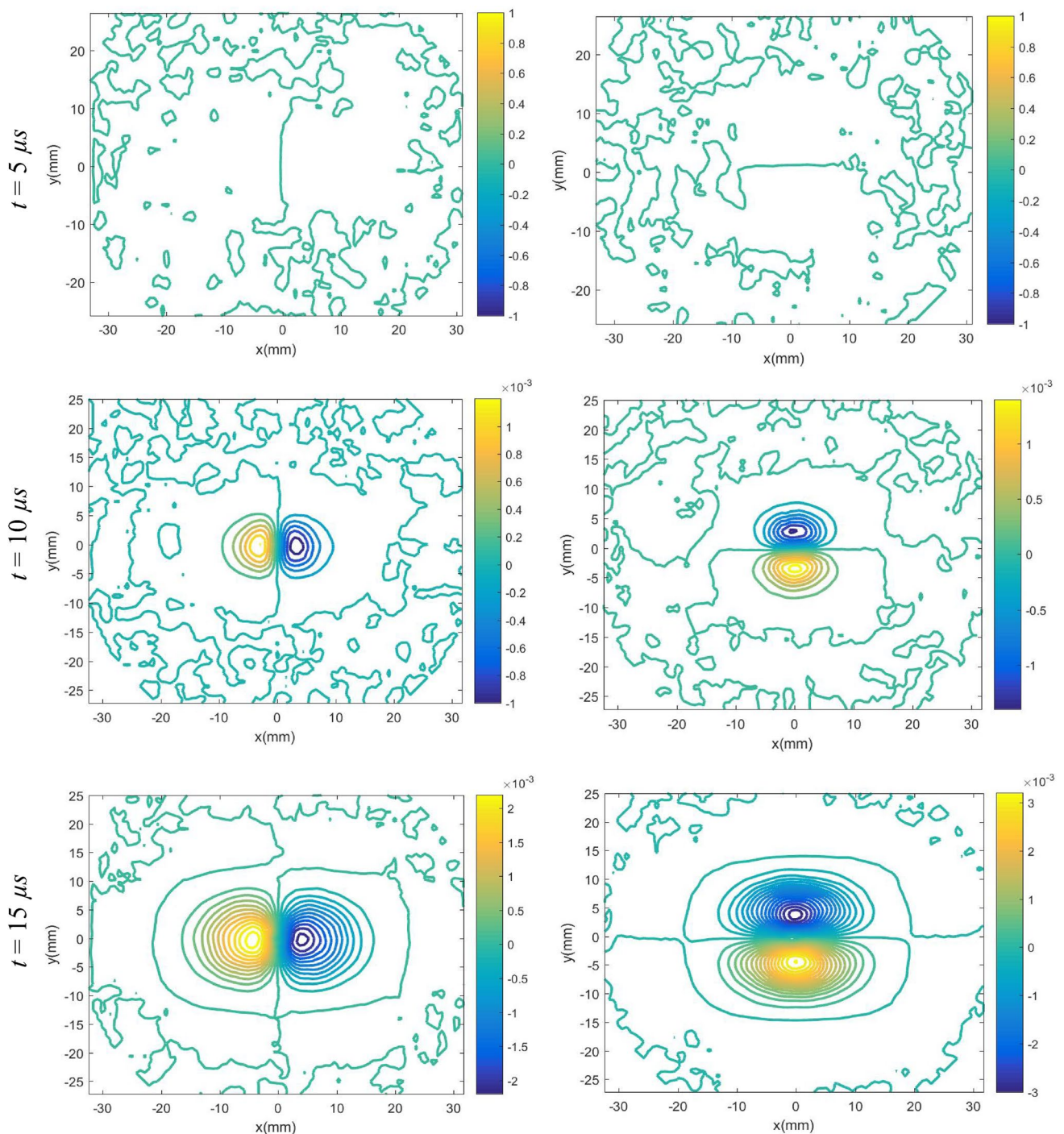

Fig. 12 Comparison of experimental (solid symbols) results with finite element simulations (solid line) at different time instants

Fig. 13 Evolution of slopes $w_{,x}$ (left column) and $w_{,y}$ (right column) contours for a clamped unidirectional CFRP plate subjected to central impact. Note: (0, 0) is made to coincide with the impact point. Fiber direction is in the horizontal direction. Contour increments $= 2 \times 10^{-4}$ rad (also see supplementary animation of files)

conjunction with HFLI scheme are plotted in Fig. 19. The corresponding contours of out-of-plane displacements (w) at 0.26 μm increment are shown in Fig. 19b, d, f. At $t = 5$ μs, a sub-micron magnitude peak deformation of ~0.2 μm was recovered at the impact point. The noise level in the

reconstructed surface profile at this time instant is relatively higher than the isotropic counterparts due to a combination of extremely small out-of-plane deformations and material anisotropy. Further, it can be observed that at the same time frame, the out-of-plane deformations of quasi-isotropic
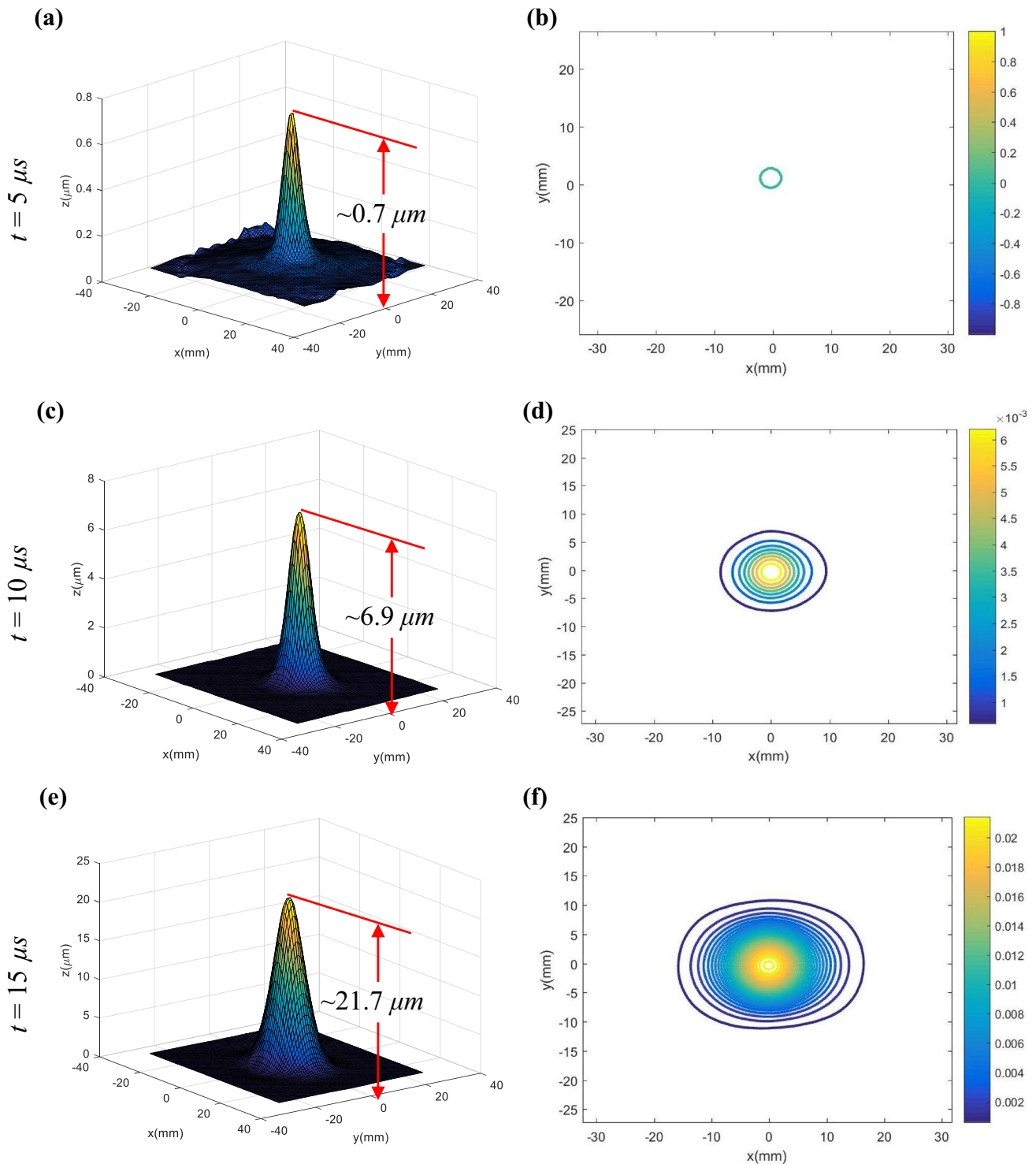
Fig. 14 Evolution of surface topography of unidirectional CFRP plate at a few select time instants. Left column: reconstructed 3D surface; right column: out-of-plane displacement (w) contours (0.8 μm incre- ment). Note: (0, 0) is made to coincide with the impact point. Fiber direction is in the horizontal direction (also see, supplementary ani- mation of files)

CFRP plate are much smaller than those of unidirectional CFRP counterpart, although they are both subjected to the same impact velocity. This is consistent with the higher

stiffness components of the quasi-isotropic CFRP plate rela- tive to the unidirectional counterpart of the same number of plies. The out-of-plane deformations along $x = 0$ at selected

Fig. 15 The measured surface profiles for a clamped unidirectional CFRP plate subjected to central impact (see "Appendix" for experimental error estimates)
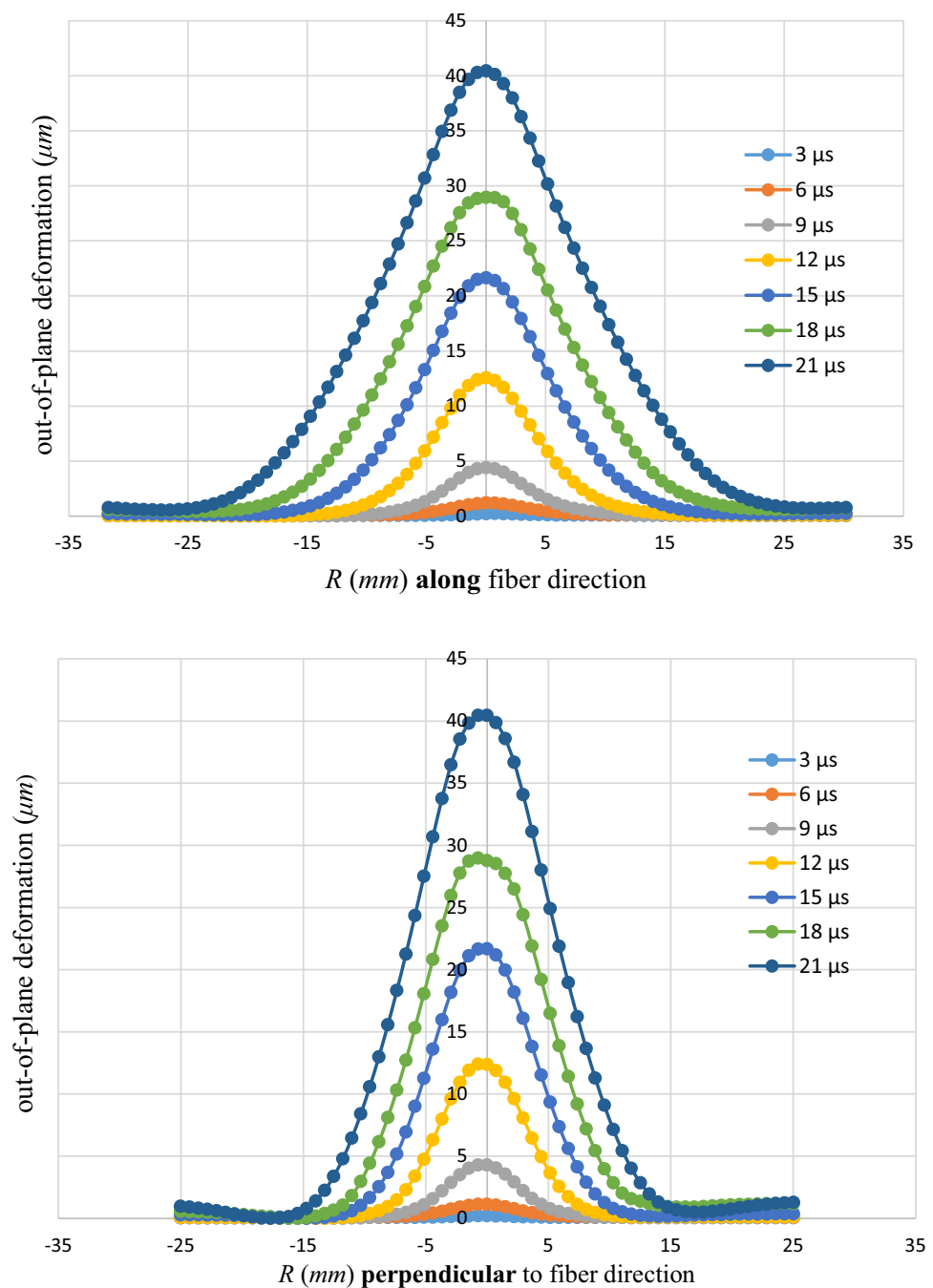
time instants are plotted in Fig. 20 and the deformations at $t = 3$ μs and $t = 6$ μs are rather small. This is different when compared to deformations of PMMA at the same time instant, although the PMMA plate studied was thicker (8.5 vs. 4.5 mm) than the CFRP plate.

To compare the histories of maximum out-of-plane deformation (w_{max}) of PMMA, unidirectional CFRP and quasi-isotropic CFRP plates, all impacted with a striker velocity of 8.5 m/s, the experimental data are plotted in Fig. 21. The deformations increase in each of these cases monotonically during the window of observation. The deformations for

PMMA are the largest at each time instant even though it is twice as thick as the CFRP plates. The magnitude of deformation of the PMMA plate is followed by unidirectional CFRP and quasi-isotropic CFRP, respectively.

Concluding Remarks

A full-field optical method to quantitatively visualize both out-of-plane deformations and in-plane stresses in thin composite plates subjected to lateral impact has been outlined.
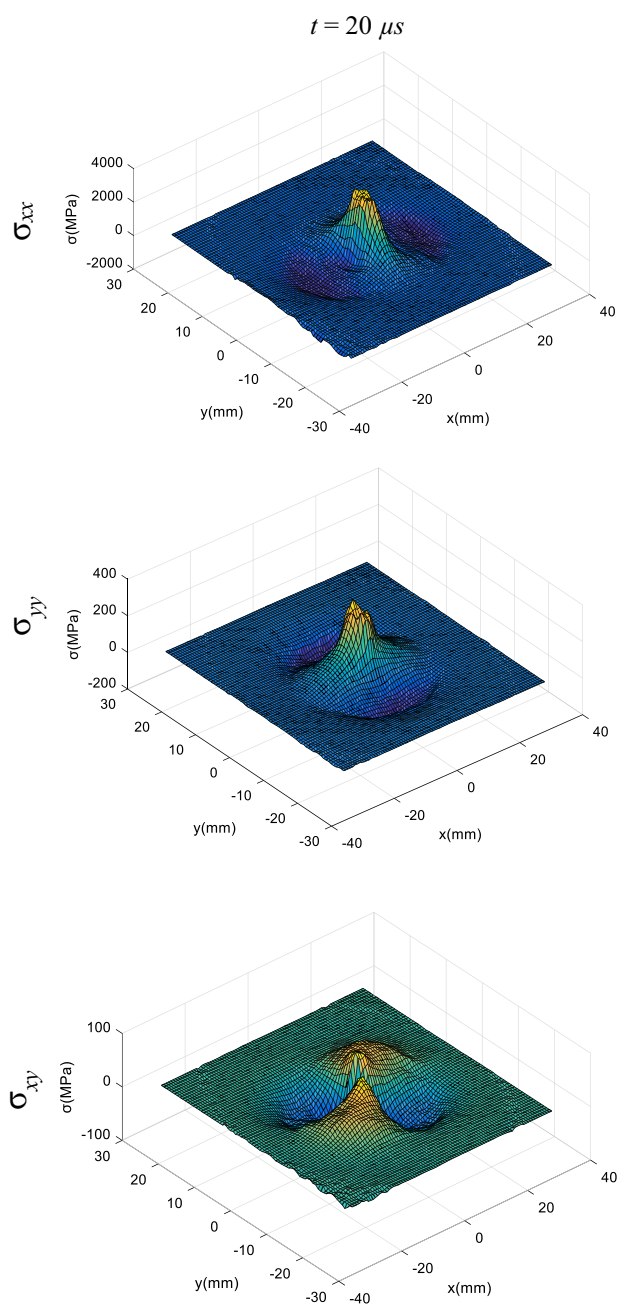
$t = 20~\mu s$

Fig. 16 Estimated stresses for a circular, clamped unidirectional CFRP plate subjected to central impact. Fiber orientation is along the *x*-axis

First, the feasibility of measuring small (micro-radian) surface slopes in two orthogonal directions at microsecond temporal resolution over relatively large regions of interest (50–75 mm) has been demonstrated using r-DGS method

along with ultrahigh-speed photography. Subsequently, evaluation of micron scale out-of-plane deformations from measurements using 2D higher-order least-squares numerical integration scheme is presented and validated. The same surface slopes, differentiated numerically to determine curvatures allow estimation of in-plane stresses when used in conjunction with the classical plate theory. Thus, both out-of-plane deformations and in-plane stresses are successfully evaluated. The above approach has been demonstrated by conducting experiments on isotropic PMMA and orthotropic CFRP plates subjected to low-velocity central impact loading. The measured out-of-plane deformations are comparatively evaluated relative to computational simulations by performing elasto-dynamic finite element analyses using measured particle velocity as input. Good agreement between measurements and simulations, even when the peak values are in the sub-micron scale, are seen. The normal and shear stress components estimated from differentiated slope data in the region-of-interest reveal details of the full-field stress distribution as well as the respective peak values and their location.

# Appendix

Effect of Sub-image Size

PMMA

To verify the effect of sub-image size on surface slope measurements and subsequently the surface topography, three different sub-image sizes, 20×20, 30×30, and 40×40 pixels and step-size of 10 pixels were considered. Experimental results for the impact loaded PMMA plate at a time instant of $t = 15~\mu s$ after impact are plotted in Fig. 22. Figure 22(1) corresponds to the measured slope $\frac{\partial w}{\partial x}$ along the *x*-axis, Fig. 22(2) shows the integrated out-of-plane deformation along the radius, Fig. 22(3) shows the estimated stress component σ_{xx} along the *x*-axis, each corresponding to different sub-image sizes considered. It can be observed from Fig. 22(1) that small differences in slope data (difference between 20×20 to 40×40 pixels for maximum $\frac{\partial w}{\partial x}$ is 6.1%) for different sub-image sizes occur. It is also clear that larger sub-image size producing smoother

Table 2 Material properties of unidirectional CFRP used in finite element simulations [32]

E$_1$ (GPa)	E$_2$ (GPa)	E$_3$ (GPa)	G$_{12}$ (GPa)	G$_{23}$ (GPa)	G$_{13}$ (GPa)	ν_{12}	ν_{23}	ν_{13}	Density (kg/m^3)
152	8	8	4	2.75	4	0.34	0.45	0.34	1632

Fig. 17 Comparison of experimental results with finite element simulations. Solid lines represent values from simulations; solid symbols represent values from the experiment (see "Appendix" for experimental error estimates)
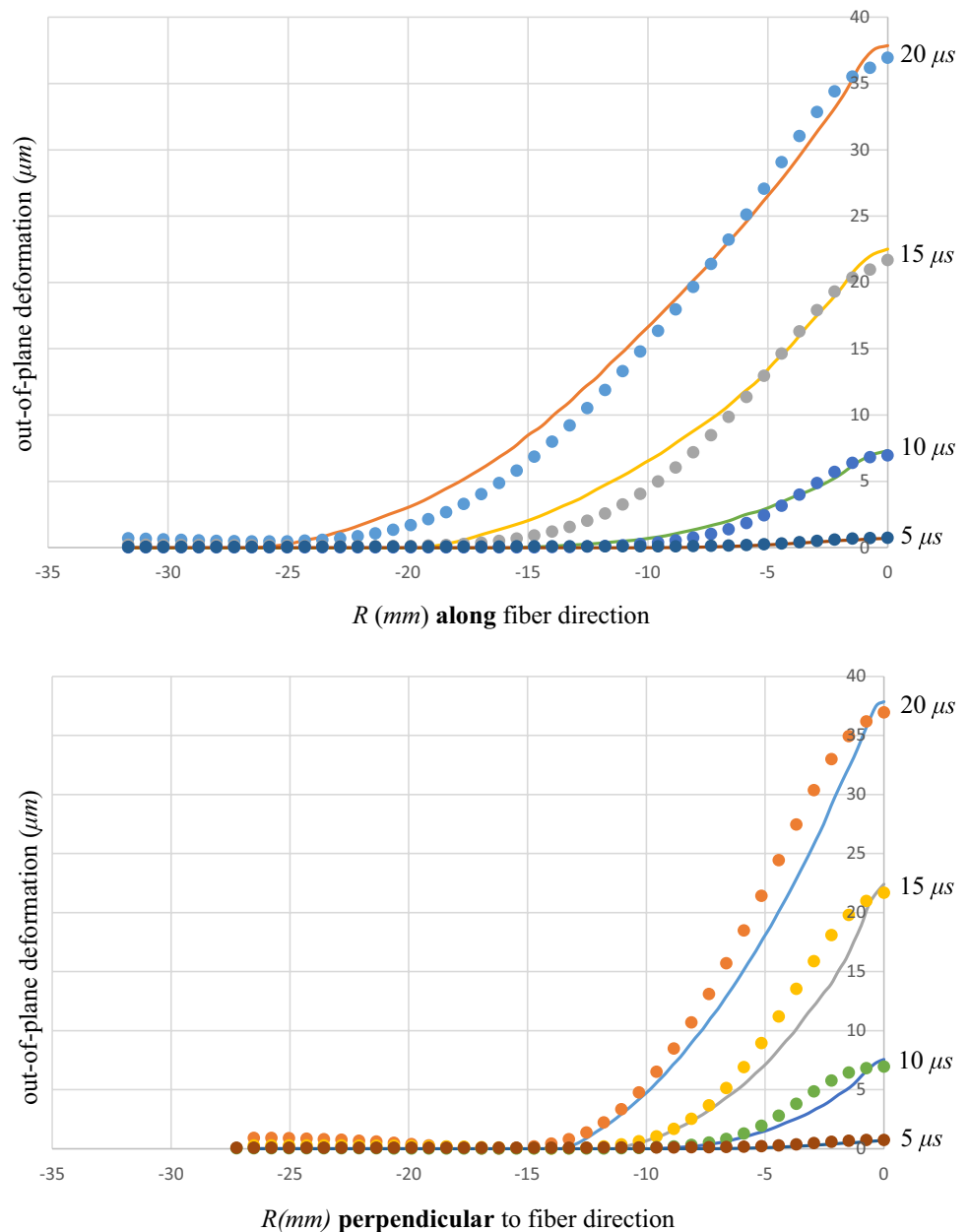
variation relative to the smaller counterpart. In Fig. 22(2), out-of-plane deformations obtained via HFLI algorithm show a smoothing effect, altering the peak value of w at the impact point by less than 1%. The estimated stress σ_{xx} was obtained from curvatures by differentiating the slope data. Once again, the effect of different sub-image sizes was observed to be acceptable. The smaller sub-image size produced noisier variation relative to the larger sub-image; approx. 13% in the peak stress value between the smallest and largest sub-image sizes is evident. Furthermore, the two different numerical differentiation schemes tested did not show significant effect on the outcome with values deviating between 4 and 5% (see Fig. 23).

CFRP

Experimental results for unidirectional CFRP along the fiber direction, again at $t = 15$ μs after impact, are plotted in Fig. 24. Similar effects of sub-image sizes can be observed in measured surface slope, and post-processed out-of-plane deformation and stress data shown in Fig. 24(1–3), respectively. The maximum (magnitude) slope difference between 20×20 and 40×40 sub-image size choice was approx. 6.9%. The larger sub-image size resulted in a smaller magnitude of maximum slopes relative to smaller sub-image size. Again, the latter produced noisier variation of slopes relative to the former. The difference in maximum out-of-plane
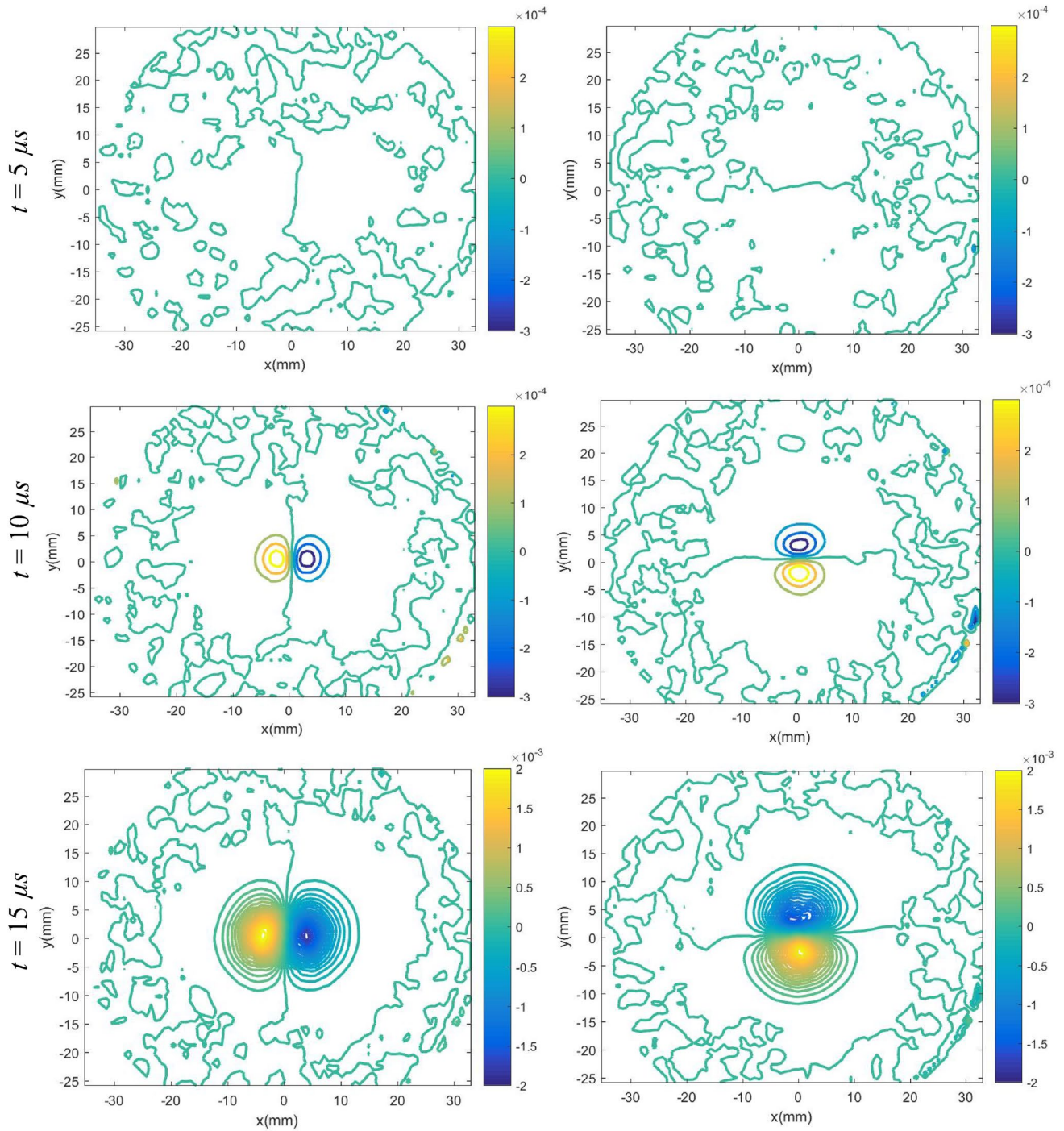
Fig. 18 Evolution of slopes $w_{,x}$ (left column) and $w_{,y}$ (right column) as contours for a clamped quasi-isotropic CFRP plate subjected to central impact. Note: (0, 0) is made to coincide with the impact point. Contour increments $= 1 \times 10^{-4}$ rad
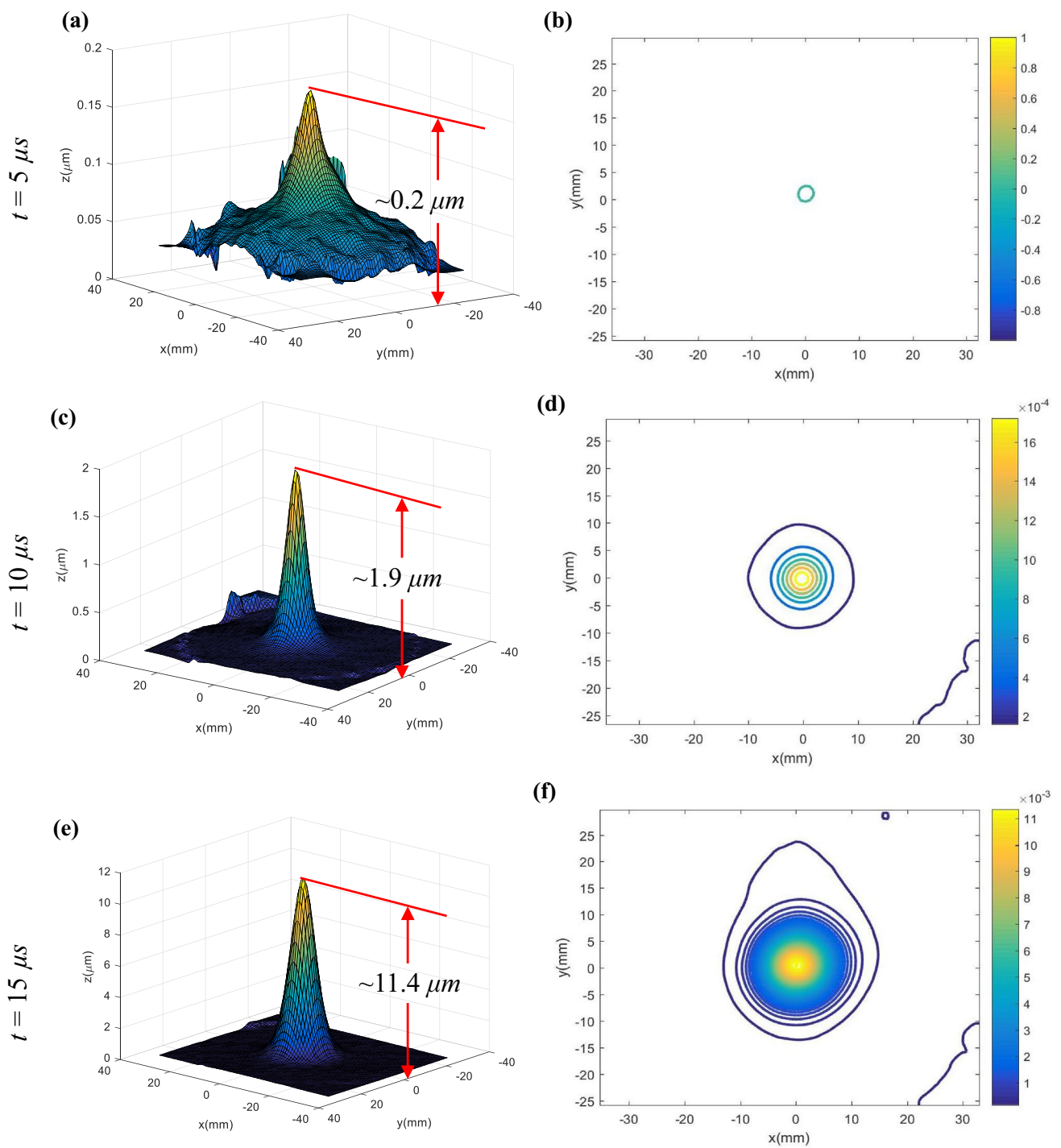
Fig. 19 Evolution of surface deformations of a quasi-isotropic CFRP plate at select time instants. Left column: reconstructed 3D surface; right column: out-of-plane displacement (*w*) contours (0.26 μm increment). Note: (0, 0) is made to coincide with the impact point

Fig. 20 The measured transient surface profiles for a clamped quasi-isotropic CFRP plate subjected to central impact
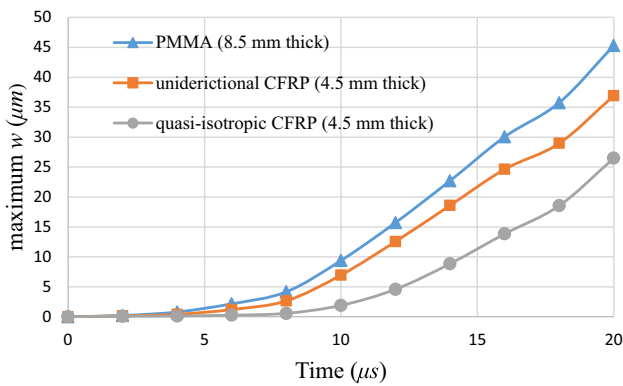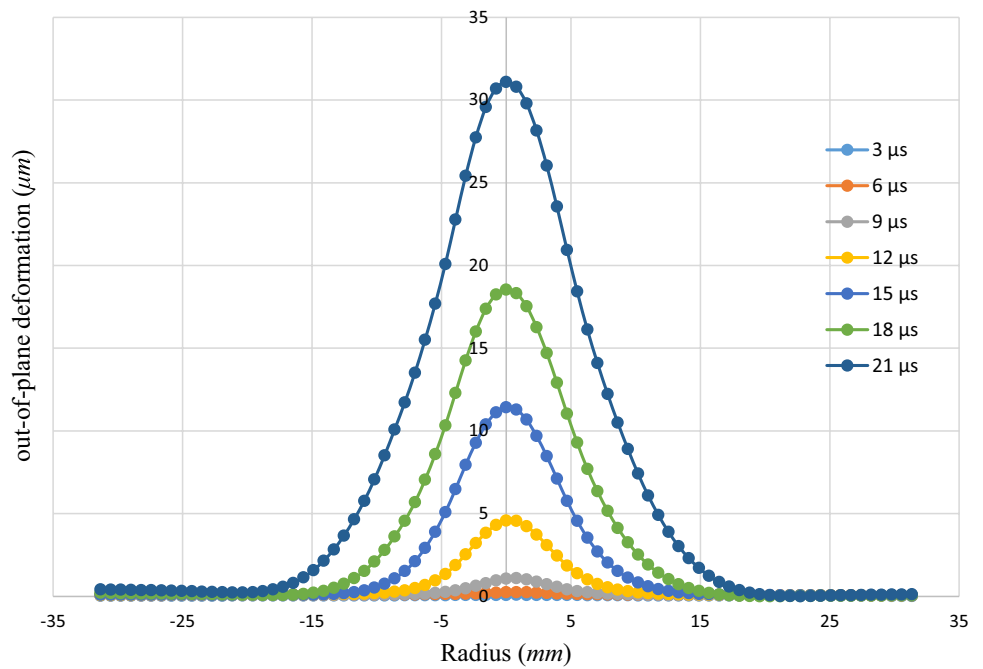

Fig. 21 Evolution of maximum out-of-plane displacement for PMMA, unidirectional CFRP and quasi-isotropic CFRP

deformations were significantly reduced ($< 0.5\%$) upon numerical integration whereas maximum stress σ_{xx} (along the fibers) showed 3.5% difference between 20×20 and 40×40 sub-image size.

Effect of Numerical Differentiation

To verify the effect of different differentiation on the estimated stress, the measured slopes of unidirectional CFRP at $t = 15$ μs were differentiated using two classical central difference schemes [33],

$$f''(x) \approx \frac{f'(x+h) - f'(x-h)}{2h} \tag{A1}$$

$$f''(x) \approx \frac{-f'(x+2h) + 8f'(x+h) - 8f'(x-h) + f'(x-2h)}{12h} \tag{A2}$$

to obtain the local curvatures, where h is the interval between two neighboring data points of f'. The stresses shown in Figs. 10 and 16 were obtained using Eq. (A1). The algorithmic error of Eq. (A1) is of order $O(h^2)$, while for Eq. (A2), the algorithmic error is $O(h^4)$ [33]. The estimated stress component σ_{xx} along the x-axis corresponding to these two formulas is plotted in Fig. 23. Evidently, the two sets of data nearly overlay with each other suggesting
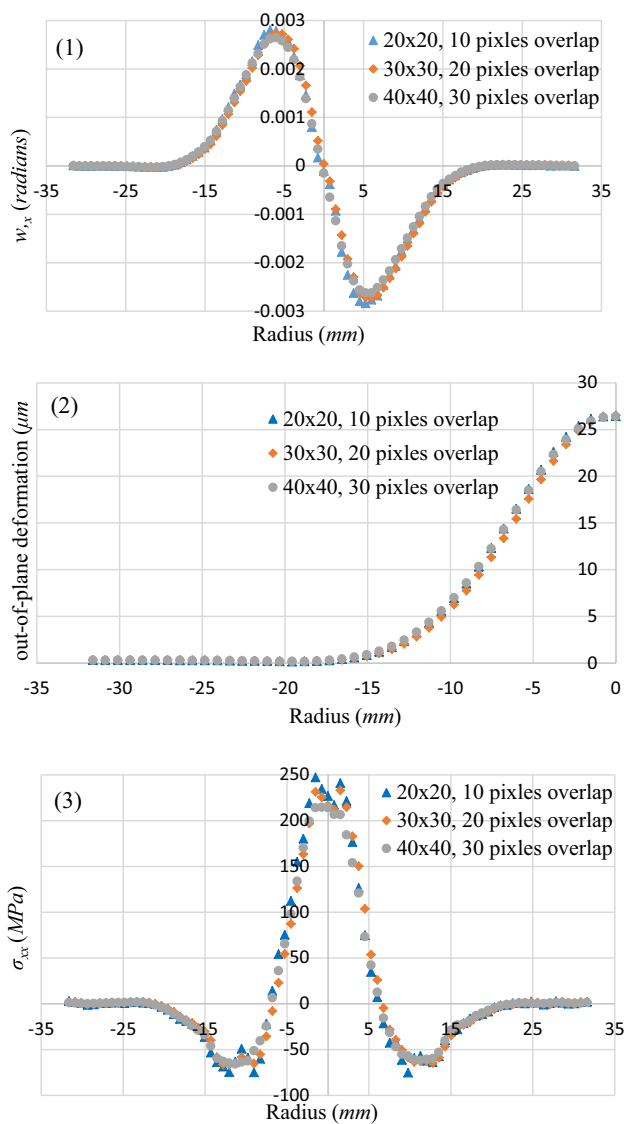
Fig. 22 Effect of sub-image sizes for PMMA at $t = 15$ μs **1** on surface slope $w_{,x}$; **2** on out-of-plane deformation; **3** on stress
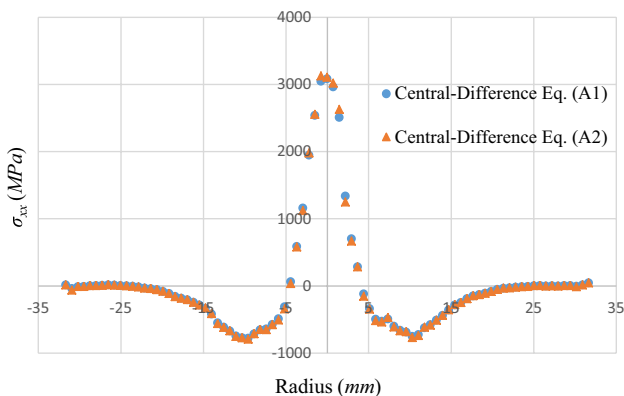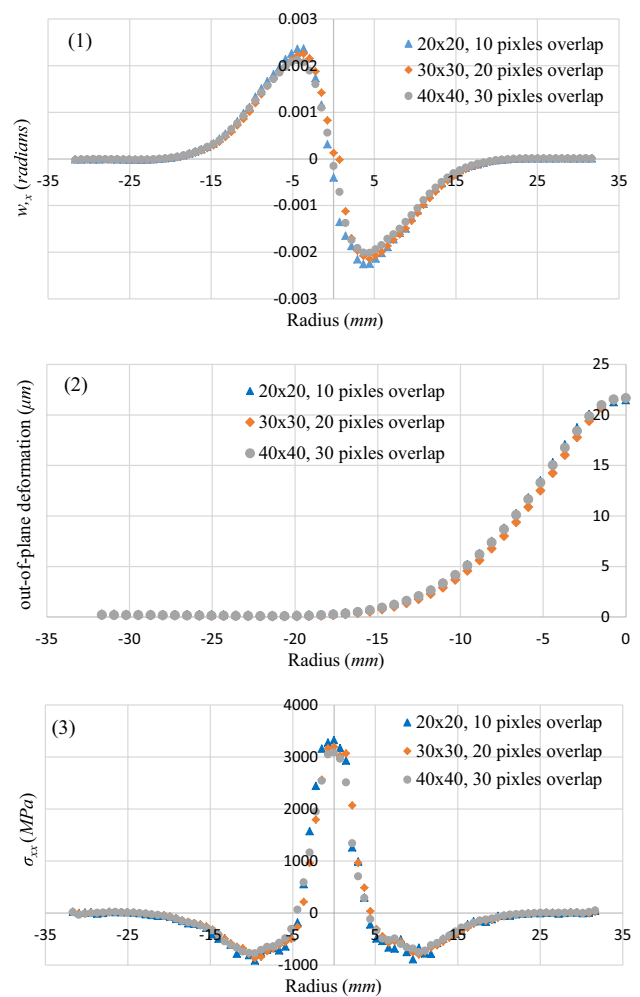

Fig. 24 Effect of sub-image sizes for unidirectional CFRP at $t = 15$ μs: **1** on surface slope $w_{,x}$; **2** on out-of-plane deformation; **3** on stress

minimum influence of the numerical differentiation scheme in the range of 4–5%.

References

1. Thomassin J-M, Jerome C, Pardoen T, Bailly C, Huynen I, Detrembleur C (2013) Polymer/carbon based composites as electromagnetic interference (EMI) shielding materials. Mater Sci Eng R 74:211–232
2. Soutis C (2005) Fibre reinforced composites in aircraft construction. Prog Aerosp Sci 41:143–151
3. Williams G, Trask R, Bond I (2007) A self-healing carbon fibre reinforced polymer for aerospace applications. Compos A 38:1525–1532
4. Lee SH, Waas AM (1999) Compressive response and failure of fiber reinforced unidirectional composites. Int J Fract 100:275–306
5. Sanchez-Saez S, Barbero E, Zaera R, Navarro C (2005) Compression after impact of thin composite laminates. Compos Sci Technol 65:1911–1919

Fig. 23 Estimated stress obtained from different numerical differentiation methods for 40×40 pixel sub-images, $t = 15$ μs

6. Walker L, Sohn M-S, Xiao-Zhi H (2002) Improving impact resistance of carbon-fibre composites through interlaminar reinforcement. Compos A 33:893–902

7. Grediac M (2004) The use of full-field measurement methods in composite material characterization: interest and limitations. Compos A 35:751–761

8. Quinn JP, McIlhagger AT, McIlhagger R (2008) Examination of the failure of 3D woven composites. Compos A 39:273–283

9. Bosia F, Botsis J, Facchini M, Philippe G (2002) "Deformation characteristics of composite laminates—part I: speckle interferometry and embedded Bragg grating sensor measurements". Compos Sci Technol 62:41–54

10. Tippur HV, Krishnaswamy S, Rosakis AJ (1991) Optical mapping of crack tip deformations using the methods of transmission and reflection coherent gradient sensing: a study of crack tip K-dominance. Int J Fract 52:91–117

11. Lee H, Rosakis AJ, Freund LB (2001) Full-field optical measurement of curvatures in ultra-thin-film-substrate systems in the range of geometrically nonlinear deformations. J Appl Phys 89:6116–6129

12. Tippur HV (2004) Simultaneous and real-time measurement of slpoe and curvature fringes in thin structures using shearing interferometry. Opt Eng 43:3014–3020

13. Ritter R (1982) Reflection moire methods for plate bending studies. Opt Eng 21:663–671

14. Cairns DS, Minguet PJ, Abdallah MG (1994) Theoretical and experimental response of composite laminates with delaminations loaded in compression. Compos Struct 24:431–437

15. Karthikeyan K, Russell BP, Fleck NA, Wadley HNG, Deshpande VS (2013) The effect of shear strength on the ballistic response of laminated composite plates. Eur J Mech A 42:35–53

16. Koerber H, Xavier J, Camanho PP (2010) High strain rate characterisation of unidirectional carbon-epoxy IM7-8552 in transverse compression and in-plane shear using digital image correlation. Mech Mater 42:1004–1019

17. Yamada M, Tanabe Y, Yoshimura A, Ogasawara T (2011) Three-dimensional measurement of CFRP deformation during high-speed impact loading. Nucl Instrum Methods Phys Res A 646:219–226

18. Pankow M, Justusson B, Waas AM (2010) Three-dimensional digital image correlation technique using single high-speed camera for measuring large out-of-plane displacements at high framing rates. Appl Opt 49:3418–3427

19. Yu L, Pan B (2016) Single-camera stereo-digital image correlation with a four-mirror adapter: optimized design and validation. Opt Lasers Eng 87:120–128

20. Pan B, Yu L, Yang Y, Song W, Guo L (2016) Full-field transient 3D deformation measurement of 3D braided composite panels during ballistic impact using single-camera high-speed stereo-digital image correlation. Compos Struct 157:25–32

21. Periasamy C, Tippur HV (2012) Full-field digital gradient sensing method for evaluating stress gradients in transparent solids. Appl Opt 51(12):2088–2097

22. Periasamy C, Tippur HV (2013) Measurement of orthogonal stress gradients due to impact load on a transparent sheet using digital gradient sensing method. Exp Mech 53:97–111

23. Periasamy C, Tippur HV (2013) A full-field reflection-mode digital gradient sensing method for measuring orthogonal slopes and curvatures of thin structures. Meas Sci Technol 24:025202

24. Jain AS, Tippur HV (2016) Extension of reflection-mode digital gradient sensing method for visualizing and quantifying transient deformations and damage in solids. Opt Laser Eng 77:162–174

25. Miao C, Sundaram BM, Huang L, Tippur HV (2016) Surface profile and stress field evaluation using digital gradient sensing method. Meas Sci Technol 27:095203

26. Tippur HV (2006) Optical techniques in dynamic fracture mechanics. In: Shukla A (ed) Dynamic fracture mechanics. World Scientific Publications, Singapore

27. Southwell WH (1980) Wave-front estimation from wave-front slope measurements. J Opt Soc Am 70:998–1006

28. Huang L, Idir M, Zuo C, Kaznatcheev K, Zhou L, Asundi A (2015) Comparison of two-dimensional integration methods for shape reconstruction from gradient data. Opt Laser Eng 64:1–11

29. Li G, Li Y, Liu K, Ma X, Wang H (2013) Improving wave front reconstruction accuracy by using integration equations with higher-order truncation errors in the Southwell geometry. J Opt Soc Am A 2013:1448–1459

30. Bauchau OA, Craig JI (2009) Kirchhoff plate theory. In: Bauchau OA, Craig JI (eds) Structural analysis. Solid mechanics and its applications. Springer, Dordrecht, pp 819–914

31. Bedsole R, Tippur HV (2013) Dynamic Fracture characterization of small specimens: a study of loading rate effects on acrylic and acrylic bone cement. J Eng Mater Technol 135:031001–031010

32. Tran T, Simkins D, Lim SH, Kelly D, Pearce G, Prusty BG, Gosse J, Christensen S (2012) Application of a scalar strain-based damage onset theory to the failure of a complex composite specimen. In: 28th Congress of the International Council of the Aeronautical Sciences, Brisbane, Australia

33. Mathews JH, Fink KK (2004) Numerical methods using Matlab, 4th edn. Prentice-Hall Inc, Upper Saddle River